PiP-plex: A Particle-in-Particle System for Multiplexed Quantification of Secreted Proteins by Single Cells

Félix Lussier[1,2,3*], Byeong-Ui Moon[3], Mojra Janta-Polczynski[3], Yonatan Morocz[1,2], Fabian Svahn[1,2], Molly Shen[1,2], Ljuboje Lukic[3], Lidija Malic[1,3], Teodor Veres[3], Andy Ng[1,2] and David Juncker[1,2*]

[1] Biomedical Engineering Department, McGill University, 3775 Rue University, Montréal, QC, H3A 2B4, Canada

[2] Victor Phillip Dahdaleh Institute of Genomic Medicine, McGill University, 740 Dr. Penfield Avenue, Montréal, QC, H3A 0G1, Canada

[3] National Research Council of Canada, 75 de Mortagne, Boucherville, QC, J4B 6Y4, Canada

* Corresponding Authors: Felix.Lussier@cnrc-nrc.gc.ca, David.Juncker@McGill.ca

Abstract

Cell signaling is modulated by the secretion of various proteins, which can be used to infer a cell's phenotype. However, these proteins cannot be readily detected in multiplex by commonly used methods at the single-cell level. Here, we present a particles-in-particle (PiPs) concept comprising fluorescence intensity barcoded microparticles (BMPs) co-entrapped with a single cell inside an alginate hydrogel particle for multiplex protein secretion analysis (PiP-plex) and imaged by confocal microscopy. We developed a seven-plex fluorescent barcoding and concomitant sandwich immunoassay in PiPs with limits of detection ranging from 0.8 pg mL^{-1} to 2 ng mL^{-1} depending on the protein. PiP-plex assays were benchmarked with bulk immunoassays and found to rival or outperform them. We applied PiP-plex to analyze protein secreted by THP-1 cells upon exposure to lipopolysaccharide and detected varying cell responses, with a significant increase in MIP-1α, TNF-α and IL-17A. Multivariate analysis revealed that the majority of stimulated cells secreted either MIP-1α or IL-17A, while other cytokines were typically co-secreted. PiP-plex enables the analysis of ~1000 cell h^{-1}, while retaining >90 % cellular viability, showcasing its potential for characterizing cells and cell-based therapeutics for cancer immunotherapies.

Introduction

Cell signaling plays a central role in health and disease, as cells secrete proteins and vesicles to communicate and orchestrate collective behavior. For instance, immune cells encountering pathogenic material or stimulated by neighboring cells can expand into a heterogeneous repertoire of functionally distinct types to modulate the immune response. These diverse cellular phenotypes are reflected in the composition and abundance of secreted cytokines and chemokines,[1-3] key modulators of immune functions. Hence, cell secretion contains promising information for fundamental cell biology studies, as well as for diagnostic and therapeutic monitoring. However, commonly employed bulk-type measurements only record ensemble averages and fail to capture single cell heterogeneity known to drive systemic responses.[4] Furthermore, so-called polyfunctional cells that co-secrete multiple proteins, have been identified as major contributors to the efficacy of immunotherapy,[5] underlining the importance of detecting single cell protein secretion signatures.

Quantification of single cell protein secretions is typically performed by segregating cells in microfluidic chambers,[1, 2] water-in-oil (W/O) droplets,[6-12] or hydrogels.[13-16] Within the confined space, secreted proteins are captured on arrays of capture antibodies (cAb),[17] or on nano-[7-9] to micrometer-sized[10, 18, 19] beads followed by incubation with fluorescently labeled detection antibodies (dAbs), forming a sandwich immunoassay. Microfluidic chips are used to manipulate and sort W/O droplets post-assay, based on the fluorescence signal of droplets and cells.[20, 21] However, sandwich immunoassays performed in W/O droplets co-encapsulate labeled dAb that contribute to a high background, which limits the sensitivity and multiplexing capacity. Moreover, meticulous optimization of droplet size for optimal cell viability, which depends on the cell type, may be required.[22] Many limitations were mitigated by technologies employing hydrogels to trap cells for immunoassays. Cells are either directly entrapped inside the hydrogel matrix during gel formation using a microfluidic droplet generator,[6, 23] or trapped within a templated cavity (e.g. nanovials[15, 24, 25]) that circumvent the need for microfluidic droplet generators. Due to the porosity of hydrogels and the open geometry of nanovials, assay reagents for single cell immunoassays can be easily added and washed while maintaining cell viability. Additionally, the droplets are compatible with flow cytometry (FCM) for high throughput quantification and sorting by fluorescence-activated cell sorting (FACS).

Droplets and nanovials can be combined with downstream sequencing to correlate protein secretion with gene expression using DNA-barcoded antibodies.[13, 14] In this case, multiplex secretion profiles can be accomplished, but cells are not retrievable. Moreover, while multiplexed fluorescent readouts for secreted proteins can preserve cell viability and provide immediate results, they remain challenging due to spectral overlap between fluorescent dyes, as well as low concentrations and weak signals. As a result, the level of multiplexing remains

low, whereas only two[26]- or tri-plex[6] assays have been reported to date. Spatial segregation of secreted antibodies inside a microfluidic chamber patterned with antibody arrays can increase multiplexing and is now commercially available as a single cell barcoded chip (SCBC).[2] However, the process is reliant on complex, application-specific instrumentation, costly consumables and cells are not retrievable for further analysis.

We recently reported the development of intensity barcoded microparticles (BMPs) enabling high multiplex sandwich immunoassay (MSA) for quantification of proteins by FCM (see Supplementary Note 1).[27, 28] By using DNA oligos as building blocks, double-stranded DNA (dsDNA) oligos harboring both a 5' biotin and a 3' fluorescent dye modifications were bound to streptavidin-coated microparticles in the presence of biotinylated cAbs to serve as an immunoassay support. Using this approach, we demonstrated that the amount of labeled dsDNA supplied to the microparticles was stoichiometrically recapitulated on the surface of the particles, enabling the generation of over 500 distinct multicolor BMPs. These BMPs were used for bulk immunoassays without further encapsulation.

In this work, we introduce a novel particle-in-particle (PiPs) system for multiplex quantification of proteins secreted by single cells, referred to as PiP-plex (Figure 1A) using BMPs, well-established microfluidic droplet generators, and a conventional fluorescence confocal laser scanning microscopy (CLSM). We co-encapsulate single cells with a panel of BMPs, each functionalized with an antibody against a different cytokine, into permeable alginate hydrogel particles using droplet microfluidics to generate PiPs. The BMPs entrapped in PiPs are used to assess the functional diversity of single cells via their cytokine secretion. The permeable alginate permits diffusive perfusion and rinsing of assay reagents for MSAs, encapsulation in oil for single cell incubation, and subsequent oil removal while preserving cell and BMP association, all while effectively excluding large molecules weighing over 2 MDa. We developed a processing pipeline that includes imaging of PiPs and BMPs using CLSM, segmenting BMPs in 3D data, decoding them, and quantifying the bound cytokine concentration. Using PiP-plex sandwich immunoassays, we quantified up to seven proteins secreted by single cells. As a proof-of-concept, we assessed the functional diversity of THP-1 macrophage (Mφ)-like cells upon stimulation by lipopolysaccharide (LPS), identifying multiple distinct cell phenotypes while preserving cell viability.

Results and discussion:

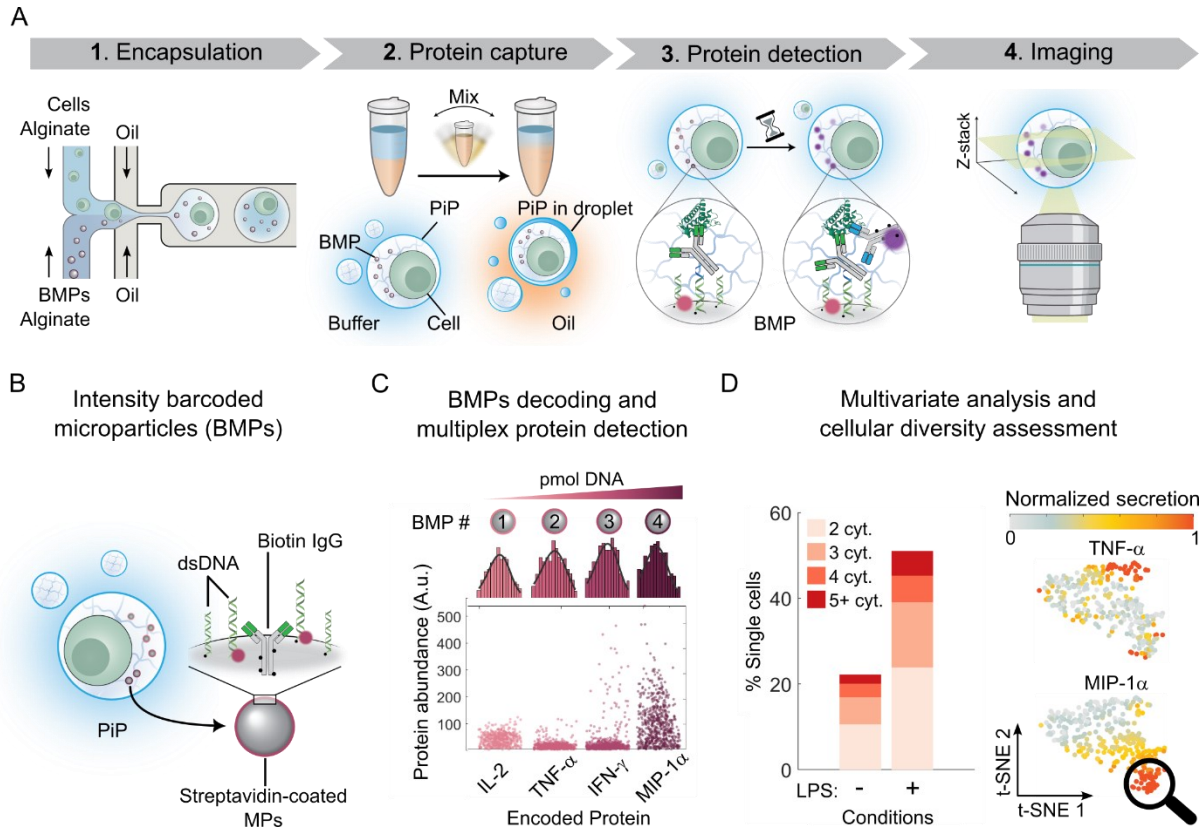

Figure 1: Multiplexed quantification of proteins secreted by a single cell with PiP-plex. (**A**) Schematic representation of the PiP-plex pipeline including four key steps: **1.** Co-encapsulation of BMPs along with a single cell and soluble alginate in W/O droplets, crosslinking of alginate to form particles-in-particle (PiPs) hydrogel entrapping a single cell. Droplets are coalesced, and PiPs are isolated, washed, and stored in the desired medium. **2.** The assay is performed by exchanging the medium with assay buffer containing a stimulating agent (e.g. LPS), after which PiPs are re-encapsulated in W/O droplets for incubation and capture of secreted proteins by the corresponding BMPs. **3.** PiPs are washed and sequentially incubated with a cocktail of dAbs and fluorescently labeled streptavidin. **4.** PiPs are added into an observation well-plate and imaged by CLSM. (**B**) A generalized construct of BMPs composed of biotinylated and fluorescently labeled dsDNA and biotinylated IgG adsorbed onto streptavidin-coated microparticles (MPs). (**C**) BMPs are barcoded by increasing the amount of labeled dsDNA on their surface and used for multiplex detection of secreted proteins by decoding the BMPs and measuring the detection antibody signal on each BMP entrapped in PiPs. (**D**) Data generated by PiP-plex enables the assessment of cellular diversity, such as the number of individual cytokines secreted by single cells and multivariate analysis for further exploration.

BMPs can be automatically localized and decoded by CLSM: BMPs for immunoassays are commonly used in FCM, where they can be individually decoded and employed for assay readout. However, FCM cannot be directly used to decode and analyze PiPs containing multiple BMPs, requiring an image-based method to spatially resolve individual BMPs. While imaging FCM may be available, the low resolution in *Z-axis* fails to meet the requirements for spatially resolving stochastically distributed BMPs, as well as for quantitatively decoding both the barcode and the immunoassay signal. Conversely, CLSM features high spatial resolution in *XYZ*. Hence, we explored its use for PiP-plex by imaging PiPs, decoding all entrapped BMPs, and quantifying their fluorescence signal. Furthermore, we compared our assay results to non-encapsulated BMPs analyzed by FCM.

First, we generated single-color BMPs using double-stranded encoder oligos ($dsEO_i$) harboring a single fluorescent dye encoder. Each dye encoder was conjugated to the 3' end of a 21-nucleotides (nt) DNA oligo (EO_i) and annealed to a complementary 5' biotinylated oligo (SO) to produce $dsEO_i$. We incorporated a non-fluorescent encoder oligo (EO_0) to balance and conserve the overall amount of dsEOs bound to the particles (Figure S1A; Supplementary Note 1). Then, mixtures of $dsEO_i$ and $dsEO_0$ along with biotinylated IgG were bound onto streptavidin-coated microparticles to form the BMPs (Figure 1B, Figure S1B). Here, the fluorescence intensity encoded in the BMPs was used for protein encoding, while IgGs enabled protein quantification by immunoassay (Figure 1C), allowing the assessment of single-cell secretion signatures and cellular diversity (Figure 1D). We used both, conventional FCM dyes (FAM, Cy3 and Cy5) and microscopy-favored dyes (ATTO488, ATTO550 and AF647), known for their higher irradiance and photostability, to generate BMPs, while employing similar excitation/emission configurations for analysis (Figure S2A). For each single-color BMP, four standards were generated by varying the $dsEO_i$:$dsEO_0$ ratio. In all cases, we fixed the total amount of double-stranded oligos ($dsEO_0$ + $dsEO_i$) to 90 pmol, based on our previous work.[27] BMPs were electrostatically immobilized on a poly-L-lysine (PLL) coated coverslip to minimize Brownian motion and drift during imaging (Figure 2A). Upon imaging, we noted a highly homogeneous background caused by scattering at various excitation wavelengths, particularly during Ex/Em at 561/590 nm (Figure S2B), which we attributed to the solid magnetic core of the microparticles. Minimal background/scattering of the BMPs was observed with non-paramagnetic beads, confirming our hypothesis (Figure S2C). We used this intrinsic, homogeneous scattering signal to locate each BMP centroid by applying a 3D spherical Hough transform directly to the volumetric data (*Z*-stack) of the signal (Figure 2B).[29] We then generated and applied a 3.0 µm diameter spherical mask to the uniformly-sized BMPs (~2.8 µm, size distribution < 3 %), with each mask centered on the detected spheroid, followed by image segmentation using a 3D watershed algorithm. The resulting masks were used to

integrate the volumetric fluorescence intensity of each BMP for each fluorescence channel. The usage of the intrinsic 561/590 nm signal to segment all individual BMP overcomes the challenges related to the segmentation of the BMPs exhibiting low fluorescence intensity barcodes with insufficient signal intensity for reliable segmentation. BMPs generated with dyes employing the 561/590 nm Ex/Em configuration (e.g., ATTO550 and Cy3) did not interfere with the segmentation. The single BMP fluorescence signals measured by CLSM were consistent with the ones obtained by FCM (Figure 2C).

Results showed that for both FCM and CLSM, the ATTO dyes and AF647 exhibited higher brightness and monotonic increase in signal upon increasing the $dsEO_i$:$dsEO_0$ ratio, whereas we noted a deviation in linearity at high $dsEO_i$:$dsEO_0$ ratio for Cy3 and Cy5, attributed to self-quenching of the dyes (Figure S3). For all tested dyes, the BMP signals in FCM and CLSM were correlated with Pearson's *r* values ranging from 0.84 to 0.99 (Figure S4). The coefficients of variation (%CV) were smaller for CLSM compared to FCM across all dyes, and AF647 showed the lowest variation (~6% CV) (Figure S5A-B). Taken together, these results establish CLSM as a reliable readout of BMP barcodes.

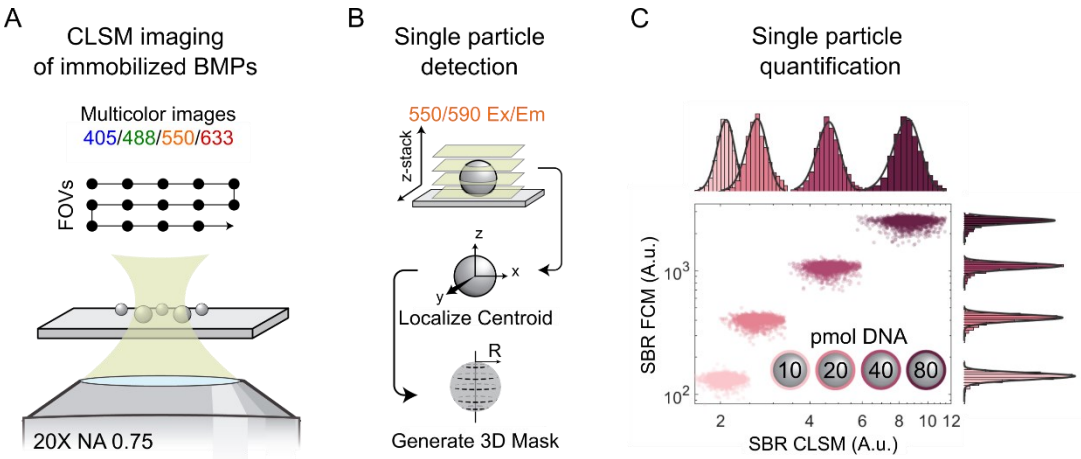

Figure 2: CLSM segmentation and decoding of BMPs directly in 3D. (**A**) Multicolor imaging of immobilized PiPs by CLSM. Multiple fields of view (FOVs) are acquired, each including multicolor *Z*-stack. (**B**) Single particle detection by CLSM. Each BMP centroid is directly localized in 3D via a spherical Hough transform on the 561/590 nm Ex/Em Z-stack images. Spherical masks with a radius *R* of 1.5 µm are centered on each BMP centroid and applied to assess the volumetric fluorescence intensity of BMPs in each fluorescence channel. (**C**) Single-particle quantification of single-color BMPs fluorescence by CLSM in 3D, compared to FCM (n > 5000 BMPs per barcode).

Novel BMPs construct improves single-color barcoding capacity and enables reliable antibody encoding for sandwich immunoassay: ELISA antibody pairs are commonly supplied as a pristine antibody to be immobilized on a solid support for analyte capture (cAb), and a biotinylated Ab intended for detection (dAb), which facilitates the subsequent binding of fluorescently or enzymatically labeled streptavidin (SA) for signal generation. In our previous efforts to generate BMPs for MSAs, we reversed the dAb and cAb by immobilizing biotinylated IgG on the surface of the MPs (Figure S1), while pristine IgGs were used as dAbs, requiring a different strategy to generate the assay signal.[27] The co-immobilization of biotinylated cAb and dsEOs for barcoding introduced a binding competition between cAb and dsEOs that was not previously considered. Such competition could skew either cAb density and/or dsEOs density, affecting assay performance and barcoding accuracy.

To reduce binding competition, we introduced a new strategy that immobilizes only dsEOs, which are used for both barcoding and subsequent antibody immobilization by hybridization (Figure 3). In conjunction with our previously used SO, we introduced a 5'-biotinylated oligos composed of 42 nt, referred to as capture oligo (CO), possessing both the complementary sequence to the EO_i and an additional 21 nt sequence (Figure 3A). Both CO and SO were annealed to their respective EO_i to generate pairs of $dsEO_i$, including a predefined ratio of double stranded spacers termed as $dsSO_i$ and double stranded capture oligos ($dsCO_i$) with the additional 21 single-stranded nt for anchoring oligo-conjugated cAbs (Figure 3A). The usage of $dsSO_i$ in conjunction with $dsCO_i$ enables predictable surface coverage and anchoring points density within the $dsEO_i$. We fixed the total amount of $dsCO_i$ and $dsSO_i$ to 20 and 70 pmol, respectively, for each $dsEO_i$ based on previous investigation using similar DNA-based construct for MSA.[28] We observed that removing the biotinylated cAb during the binding of dsEOs to the MPs resulted in an overall increase in the number of dsEOs bound to the MPs' surface (Figure S6). We found that AF647-labeled oligos exhibited the lowest %CV across all barcodes in CLSM, and used them to generate the BMPs with varying $dsEO_{AF647}$:$dsEO_0$ ratios of oligo-conjugated cAbs (cAb_{oligo}; Figure S6A), which were subsequently immobilized through pull-down hybridization. The resulting cAb-BMPs, characterized by both FCM and CLSM (Figure S6B-C), exhibited an increase in signal for the cAb_{oligo} construct compared to the original co-adsorbed biotinylated antibody (cAb_{biotin}), while preserving high correlation (Pearson's r = 0.99; Figure S6D). All AF647 barcodes generated with the novel construct had a lower %CV when compared to the BMPs generated by co-adsorbing biotinylated cAb (Figure S7).

Interestingly, after normalizing the AF647 signal of individual cAb-BMPs by their scattering signal (561/590), we observed a significant reduction in variance (Figure 3B) and the concomitant %CV for both constructs when measured by CLSM, compared to FCM (Figure S7). We hypothesized that by normalizing by the scattering of the beads, the variation in the

focal plane during imaging could be corrected, hence accounting experimentally for the positional variability of individual BMPs during imaging. The scattering-based normalization was particularly effective for AF647 for two reasons. First, the pseudo scattering signal at 590 nm was immune to bleed-through from AF647. The signal measured at 590 nm was affected by the bleed-through of dyes in the 488 channels (FAM/ATTO488), thus skewing the results. Secondly, AF647 already exhibited the lowest barcoding %CV compared to other dyes, such as Cy5, as discussed above.

Due to the quantitative recapitulation of the dsEOs proportion in solution onto MPs' surface,[27] we modeled a series of $dsEO_i$:$dsEO_0$ ratios *in silico,* exhibiting minimal overlap in the BMPs intensity distribution for both FCM and CLSM (Supplementary Note 2). The proportion of $dsEO_{AF647}$ per barcode was modeled based on the measured %CV of AF647 BMPs, with barcodes separated by ~3.5 times their expected standard deviation. We hence expected to include over 99% of a given barcode population from a normal distribution corresponding to a tolerance of less than 1 %. Using these assumptions, we predicted the generation of 3 and 5 well-separated barcodes when using cAb_{biotin} and cAb_{oligo} structure, respectively, for cAb-BMPs measured by CLSM, while the same number of barcodes was predicted for FCM (Figure S8) using either cAb_{biotin} or cAb_{oligo} structures. This barcoding capacity of single-color BMPs was the same as our previous report.[27] However, by using the AF647/590 ratio instead of the AF647 intensity to reduce the experimental %CV, we predicted the generation of 7 distinct barcodes with minimal overlap for the cAb_{oligo} structure when measured by CLSM (Figure S8), corresponding to a 1.5- to 2-fold improvement in single-color barcoding capacity. We validated experimentally the generation of 7 distinct single-color barcodes and applied their predicted intensity value for automatic decoding of the BMPs via a gaussian mixture model (GMM) by CLSM (Figure 3C). We noted this improvement in barcoding capacity solely in the case of CLSM for single-color barcode. The 7 BMPs can then be used for antibody encoding, whereas each distinct BMP served to immobilize cAb-DNA conjugate (Figure 3D). This approach enabled the encoding of a specific cAb to a given intensity value, allowing direct decoding by GMM upon imaging pooled cAb-BMPs (Figure 3E).

Next, we assessed the analytical performance of our new cAb_{oligo} structure as a bead-based support for the sandwich immunoassay. A cAb_{oligo} was generated by conjugating a 30-nt anchor oligo sequence (AO; Supplementary Table S1) to a mouse anti-goat cAb (Supplementary Table S2). Following the removal of unconjugated oligos, the cAb_{oligo} was anchored on the surface of BMPs via pull-down. We confirmed the successful hybridization of our cAb_{oligo} conjugate onto all BMPs by CLSM using a BV421-labeled goat anti-mouse dAb (Figure S9). We measured uniform BV421 labeling across all BMPs, confirming that the anchoring of cAb_{oligo} is independent of the $dsEO_{AF647}$ proportion used for barcoding. We then assayed a single cytokine (IL-5) using an anti-IL-5 cAb_{oligo} and benchmarked our performance

against FCM (Figure S10). We used a biotinylated anti-IL-5 dAb in conjunction with labeled SA to generate assay signal. Similar to our fluorescent barcoding read-out, we also used BMPs scattering at 561/590 nm to normalize the CLSM volumetric assay signal. We observed similar limits of detection (LOD) of 84 and 33 pg mL^{-1} for recombinant IL-5 in buffer using FCM and CLSM, respectively, with comparable dynamic ranges (Figure S10B). Our results indicate that the assay performance is preserved between FCM and CLSM for our cAb_{oligo} based-BMP.

Taken together, our new construct supported the generation of 7 single-color BMPs, only achievable by CLSM. Additionally, our construct can be used for sandwich immunoassay through the hybridization of cAb_{oligo} conjugates onto BMPs for protein encoding without affecting fluorescence intensity barcodes. This efficient usage of a single fluorescence channel enables the allocation of other channels for different purposes, such as cell labeling. Moreover, the use of a conventional pristine cAb enables the use of biotinylated dAb and labeled SA for assay signal generation, leveraging the use of commercially optimized ELISA antibody pairs and facilitating protein panel development.

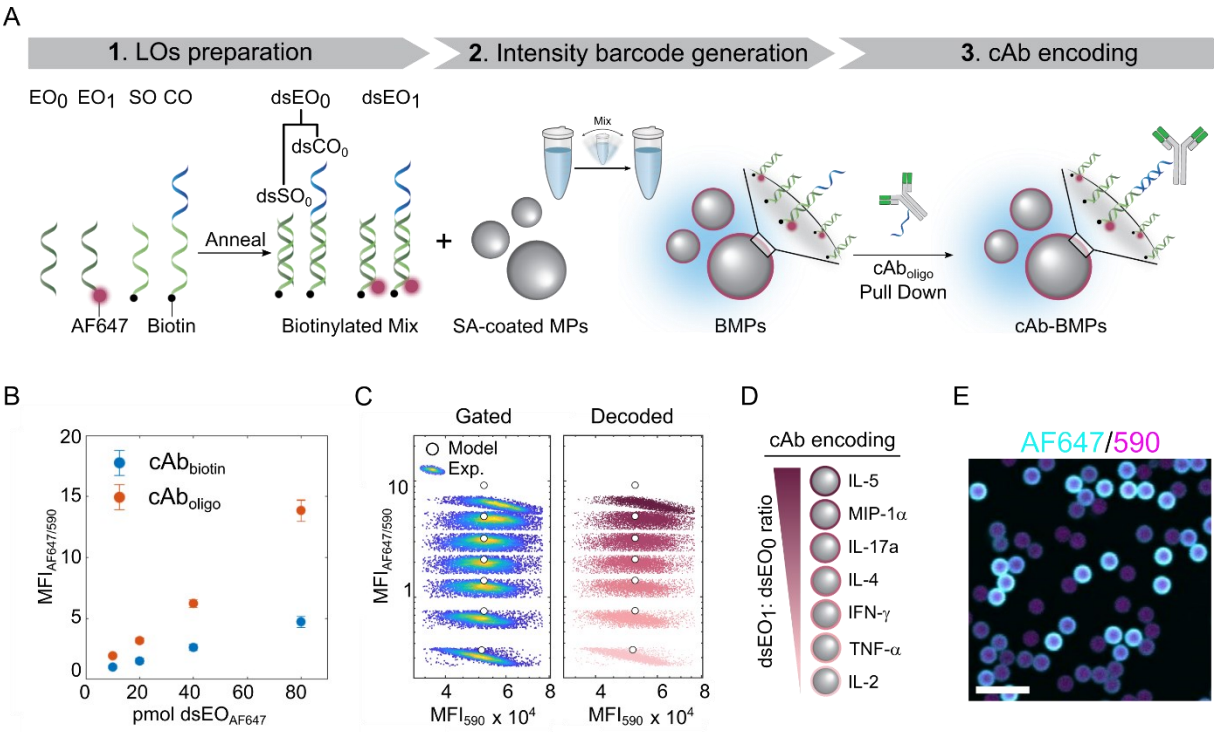

Figure 3: BMPs with high barcoding-capacity based on a cAb_{oligo} for multiplexed protein immunoassays. (**A**) Overview schematic of the three-steps in cAb-BMP assembly: **1.** Encoder oligos corresponding to unlabeled (EO_o) and fluorescently labeled oligonucleotides (EO_1) are each annealed individually in the presence of a spacer oligo (SO) and a capture oligo (CO) to generate pairs of biotinylated double-stranded encoder oligo ($dsEO_0$ and $dsEO_1$). Each $dsEO_i$ is a mixture of double-stranded spacer ($dsSO_i$) and capture ($dsCO_i$) annealed with their corresponding *i* encoder. For each $dsEO_i$, $dsSO_i$ and $dsCO_i$ were combined at a 7:2 ratio. **2.**

SA-coated MPs are then rapidly mixed with a mixture of $dsEO_0/dsEO_1$ at a specified ratio to generate the BMPs, where the $dsEO_s$ are captured onto the MPs due to the high SA-biotin affinity. By varying the ratio of $dsEO_1$:$dsEO_0$, while maintaining the overall amount of dsEOs on the surface of the MPs constant ($dsEO_1$ + $dsEO_0$ = 90 pmol), the distinct fluorescence intensity barcodes can be generated. **3.** The cAb_{oligo} conjugates are pulled down by incubating the cAb_{oligo} in presence of BMPs to capture the antibodies onto the BMPs for antibody encoding and downstream MSA. (**B**) Calibration curves of single color (AF647) cAb-BMPs measured by CLSM, normalized by the scattering of the MPs at 590 nm. BMPs were synthesized either via co-adsorption of biotinylated cAb onto the BMPs (cAb_{biotin}) or through cAb_{oligo} pull-down using the novel BMP construct (cAb_{oligo}). Mean ± S.D. (N = 3, $n \geq 5000$ BMPs) are presented. (**C**) Single-color (AF647) cAb-BMPs detected in multiplex by CLSM. Poorly segmented BMPs are gated-out based on their MFI_{590}. Individual BMPs are decoded using a Gaussian Mixture Model (GMM), initiated by the predicted intensity of the BMPs (solid white circles). (**D**) Antibody encoding of the distinct BMPs, generated at various $dsEO_1$:$dsEO_0$ ratios. (**E**) CLSM image of pooled single-color cAb-BMPs of various $dsEO_i$:$dsEO_0$ ratio. Scale Bar: 10 µm.

Droplet microfluidic generation of permeable PiPs by competitive ligand exchange: Common single cell assays are conducted in W/O droplets to isolate individual cell within an enclosed confinement. Such segregation requires the co-encapsulation of all assay reagents (e.g., labeled dAbs), which contribute to elevated background signals and, consequently, affect assay performance. In addition, enclosed confinement can negatively impact cell viability by preventing exchange of cellular reagents. Here, W/O droplets were used to segregate single cells and template alginate hydrogels, which, upon resuspension in buffer, act as permeable scaffolds for supplying and removing assay reagents. We selected alginate for its optical transparency and ease of gelation by ionic cross-linking in the presence of a divalent cation. Soluble alginate (1 % wt) was dispersed into 50 µm (~65 pL volume) W/O droplets (Figure S11) using a flow-focusing microfluidic droplet generator.[30] To ensure homogeneous cross-linking, we used a competitive ligand exchange crosslinking process employing Ca-EDTA and Zn-EDDA (Figure S11A).[31] Briefly, upon co-encapsulation of Ca-EDTA/alginate and Zn-EDDA/alginate solutions at pH 7.0, the higher affinity of EDTA toward Zn^{2+} ions induces the complexation of Zn^{2+} by EDTA and the concomitant release of Ca^{2+} ions within the droplets. Since alginate has a higher affinity for Ca^{2+} ions compared to EDDA, alginate is ionically cross-linked into hydrogels templated by the current droplet geometry. Hydrogels were then retrieved by coalescing the W/O droplets, rinsed to remove cross-linking reagents by centrifugation, and suspended in buffer (Figure S11B). To ease hydrogel visualization by CLSM, we supplemented large FITC-labeled Dextran (2MDa) which showed limited diffusion into the hydrogels (Figure S11). To assess whether alginate remained permeable to immunoassay

reagents (e.g., dAbs and labeled SA), we encapsulated antibody-coated MPs in droplets with soluble alginate to generate PiPs. We immobilized the PiPs in a microchannel and perfused them with AF488-labeled dAb and BV421 labeled SA (Supplementary Note 3; Figure S13A). Biotinylated antibodies on the surface of MPs allowed the binding of SA, while the dAb, a chicken anti-goat Ab, recognized the goat anti-mouse Ab on the MPs (Figure S13B). Upon constant flow of AF488-dAb and BV421-SA, we observed selective binding of both dAb and SA on the MPs with minimal background within the hydrogels (Figure S13C-D). We calculated a characteristic diffusion time *t* of 3.6 and 10.1 min for AF488-dAb and BV421-SA, respectively, in concordance with their respective molecular weights (MW) of ~150 kDa and 340 kDA (Figure S13E). These results validate the selective permeability of the PiPs for immunoassay reagents, but not for molecules with MW ≥ 2MDa.

Probabilities and statistics of multiple BMPs encapsulation in PiPs and multiple PiPs in droplets: We encapsulated seven BMPs into PiPs using droplet-based microfluidics at 30 000 BMPs μL^{-1} per barcode (210 000 BMPs μL^{-1} overall; Figure S14A). While the Poisson statistics predict ~14 BMPs (λ = 13.85) on average per PiP (Figure S14B), we measured on average 12 BMPs per PiP experimentally. This discrepancy between prediction and experimental results was attributed to aggregation and sedimentation of BMPs over time during the encapsulation process, skewing the encapsulation rate.

Considering the stochastic nature of BMPs encapsulation, one cannot expect to encapsulate only one of each of the seven target-specific BMPs used in our seven-plex assay. However, since we encapsulated ~ 12 BMPs per PiP, we found that on average ~35 % of PiPs contained the complete seven-plex BMPs (Figure S14C). In addition, we calculated the probability of co-encapsulating multiple BMPs with the same barcode (i.e., encoded antibody, corresponding to a technical replicate) in a PiP. By considering the concentration of single BMPs (30 000 BMPs μL^{-1}) for prediction, our results were in good agreement with Poisson statistics, with the probabilities of encapsulating 0, 1, 2 or 3 replicates of the same barcode being 22, 25, 19 and 6 %, respectively (Figure S134D).

To support downstream manipulation, such as centrifugation and resuspension, for MSA without degradation, hydrogel-based PiPs loaded with ~12 BMPs consisting of dense, paramagnetic beads needed to exhibit sufficient mechanical stability. We observed that PiPs formulated at pH 7.0 offered optimal mechanical stability, aligned with previously reported results by Bassett *et al.*[32] We then assessed if the pH and optimal cross-linking reagents were compatible with a direct immunoassay. This was accomplished by supplementing a single antigen target during PiPs generation, such that target capture and hydrogel formation would occur simultaneously within the same W/O droplet. We supplemented 100 ng mL^{-1} of recombinant IL-17A during PiPs generation at pH 7.0, and assayed antigen capture using IL-

17A encoded cAb-BMP as a single plex positive control. Assay results showed reduced affinity during antigen capture by the cAb-BMPs at pH 7.0, which was improved upon rinsing out the cross-linking reagents and raising the pH to 7.4 prior to capture (Figure S15). Hence, we implemented a rinsing step following PiP generation to ensure high affinity and immunoassay sensitivity before re-entrapping PiPs into W/O droplets, similar to templated emulsion.[33] We confirmed negligible leakage of biomolecules between mixed W/O droplets following production, or after 24 h incubation at 37 ^{o}C. However, approximately 1 in 2000 droplets exhibited leakage (Figure S16), consistent with the leakage observed in droplet-based RNA sequencing technologies.[34] We washed PiPs with medium, concentrated them by centrifugation, and re-emulsified into W/O droplets by rapidly pipetting up and down (Figure S17A). Following rinsing, and re-encapsulation of PiPs into droplets, CLSM imaging confirmed that most droplets contained a single PiP (Figure S17B), with the droplet diameter matching the size of a single PiP of ~50 µm diameter (Figure S17C). Larger droplets showed the concomitant encapsulation of multiple PiPs per droplet (Figure S17C). Overall, more than 90 % of droplets contained a single PiP, minimizing potential crosstalk between PiPs in downstream single-cell assays (Figure S17D). Our results confirm that PiPs can undergo additional processing and exhibit minimal crosstalk between PiPs, both in terms of leakage and co-encapsulation of multiple PiPs per droplets, underlining their versatility.

Benchmarking PiP-plex versus BMP multiplexed immunoassays: We applied our cAb_{oligo} assembly to generate a seven-plex cytokine panel for MSA. We selected the cytokines interleukin-2 (IL-2), IL-4, IL-17A, IL-5, tumor necrosis factor-α (TNFα), interferon-γ (IFN-γ), and chemokine (C-C motif) ligand-3 (CCL3/MIP-1α) for single cell secretion profiling due to their function as immune stimulatory, effector, regulatory and inflammatory signaling molecules.[5] We conjugated the same 30 nt sequence (AO) to all the different cAbs (Supplementary Table S2) to produce various cAb_{oligo} conjugates, which were subsequently anchored onto specific BMPs.

When we used the different cAb-BMPs for MSA, we noted a significant background signal upon incubation with BV421-labeled SA (Figure S18). We ascribed this background signal to residual SA binding sites on the BMPs which led to the direct binding of the biotinylated (multivalent) dAbs in the absence of antigen. This background signal was substantially reduced by supplementing biotin to the BSA blocking buffer (Figure S18A-B), with no effect on the intensity of fluorescent barcodes (Figure S18C). Following proper blockage, we assessed potential cross-reactivity of our antibody pairs on the cAb-BMPs (Figure S19).[35] We confirmed low cross-reactivity at both low (1 ng mL^{-1}; Figure S19A, C) and high (100 ng mL^{-1}; Figure S19B, D) antigen concentrations, validating this panel of antibody pairs for MSA. We performed MSA by incubating separately PiPs and pooled cAb-BMPs with a mixture of

antigens in buffer, followed by a cocktail of dAbs, and BV421-labeled SA. For MSA in bulk, pooled cAb-BMPs were first immobilized electrostatically using a PLL-coated well plate prior to incubation with BV421-SA. We observed that the addition of SA led to aggregation of cAb-BMPs, in an antibody dependent manner. This was attributed to the valency of the biotinylation, which negatively affected overall imaging and decoding. Immobilization of BMPs prior to labeling by SA eliminated this issue, which was not encountered with PiPs intrinsically trapping BMPs in 3D.

Depending on the antigen, PiPs exhibited slightly improved LOD compared to pooled cAb-BMPs in buffer. For instance, in the case of IL-4, a 50-fold improvement was observed, while for MIP-1α a 4-fold decrease was obtained (Figure 4). The improvement resulted from a reduction in the standard deviation of the assay on blank samples, where the calculated %CV being 101 % for assays performed in bulk and 39 % for PiP, leading to a decrease in the calculated LOD. At low concentration, the assays showed higher variation between replicates. The %CV was reduced to <10 % at concentrations above 100 pg mL^{-1} (Figure S20). The LODs of PiPs ranged from 0.8 to 2000 pg mL^{-1} on PiPs and from 0.4 to 1000 pg mL^{-1} on cAb-BMPs. Although there was an improvement in LODs, we observed a reduction in the steepness of the binding curves (i.e., a decrease in analytical sensitivity) for MSA performed in PiPs compared to bulk, which could be useful for single-cell assays. The reduction in steepness led to an increase in the dynamic range of all cytokines assayed in PiPs compared to bulk, which, in the context of a single-cell assay can be beneficial, as single-cell samples cannot be easily diluted to fall within the assay's dynamic range. Thus, a larger dynamic range is expected to help to account for cellular heterogeneity.

At high concentrations of IFN-γ, IL-4, IL-5 and MIP-1α, a reduction in assay signals was observed in PiPs compared to bulk. It is known that confinement within the hydrogel network can lead to improved protein association, while also promoting non-specific binding due to electrostatic interactions. We evaluated whether the isoelectric point of cytokines could account for improved or reduced assay performance in PiPs formulated with alginate compared to bulk, but found no generalized causal effect (Figure 4). IFN-γ, IL-4 and IL-5 possessing isoelectric points of 8.7, 9.2 and 7.8 respectively, showed the highest reduction in assay signal at high concentration rationalized by their excess of positive residue at pH 7.4 used for the assay. However, MIP-1α with an isoelectric point of 4.9, also showed reduction in assay signal.

From a physiological standpoint, cytokines are known to bind electrostatically to negatively charged glycosaminoglycan (GAG) component in the extracellular matrix.[36-38] In fact, IFN-γ,[39] IL-4,[40] IL-5[41] and MIP-1α[42] can all electrostatically bind to GAGs. Alginate contains the negatively-charged residue guluronate, an enantiomer to iduronate which is an important constituent of GAG and central to the generation of their negatively charged clusters.

Guluronate may reduce specific binding due in part to its different stereochemistry, but it still contributes to the generation of negatively charged clusters, which are associated to the non-specific binding of cytokines to alginate and the elevated background, ultimately reducing the measured SNRs at high protein concentrations. Despite this, alginate still provides key advantages such as ease of gelation, potential for chemical modification compared to agarose, ease of degradation through enzymatic reaction or by scavenging Ca^{2+} ions for cell retrieval, and enhanced MSA performance via confinement and molecular crowding. Overall, the calculated LODs are compatible with protein expression levels of single cells, with LOD <1 ng mL^{-1},[13] while empowering multiplexing.

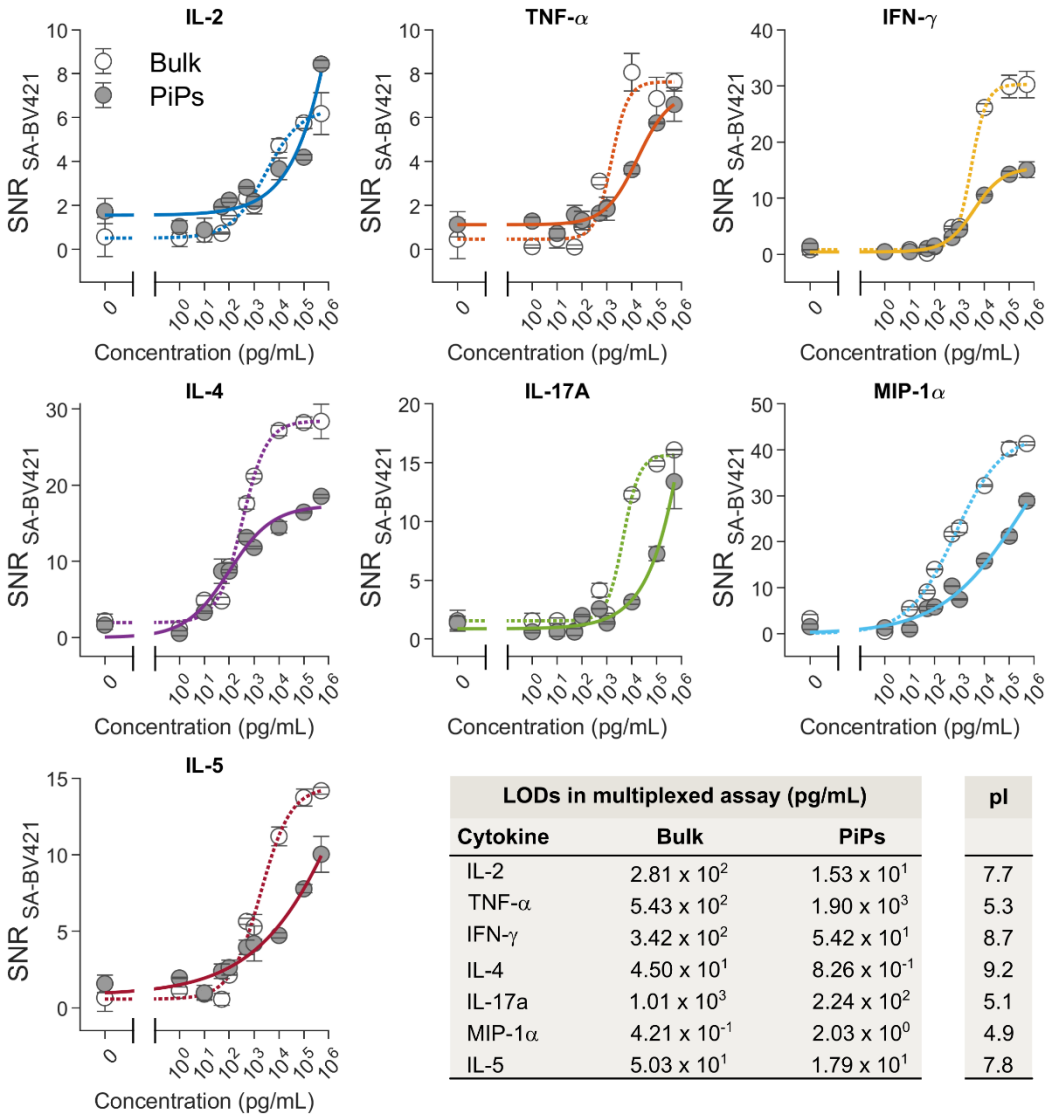

LODs in multiplexed assay (pg/mL)			pI
Cytokine	Bulk	PiPs	
IL-2	2.81×10^{2}	1.53×10^{1}	7.7
TNF-α	5.43×10^{2}	1.90×10^{3}	5.3
IFN-γ	3.42×10^{2}	5.42×10^{1}	8.7
IL-4	4.50×10^{1}	8.26×10^{-1}	9.2
IL-17a	1.01×10^{3}	2.24×10^{2}	5.1
MIP-1α	4.21×10^{-1}	2.03×10^{0}	4.9
IL-5	5.03×10^{1}	1.79×10^{1}	7.8

Figure 4: Multiplex assay binding curves acquired by CLSM for the 7-plex cytokine panel (IL-2, TNF-α, IFN-γ, IL-4, IL-17A, MIP-1α and IL-5) performed using the combined 7 cAb-BMPs in bulk (dashed lines) or formulated as PiPs (solid lines). Mean ± S.D. (n_{PIPs} = 5, n_{bulk} = 5) are presented. The plots show a fit corresponding to a four-point logistic regression. In all cases, the pooled cAb-BMPs concentration was adjusted to 100 cAb-BMPs per microliter per

samples. Calculated LODs for the different cytokines measured in bulk and PiPs with the corresponding isoelectric point (pI) are presented.

PiP-plex of cytokines secreted by single macrophages-like cells: We tested PiP-plex with the well-established THP-1 human leukemia monocytes commonly used to test single cell proteomic platforms.[2] First, THP-1 cells were differentiated into macrophage-like (Mφ) cells by 48 h incubation with 25 nM Phorbol 12-myristate 13-acetate (PMA).[43] Differentiation was confirmed by the expected change in morphology and transition from suspended to adherent cells (Figure S21). THP-1 Mφ were encapsulated with BMPs using droplet-based microfluidics as described above to form PiPs. Cell concentration was selected to maximize single cell encapsulation based on Poisson distribution, with ~45 % of PiPs containing a single cell (Figure S22A). Using calcein-AM staining, we documented >95 % cell viability (Figure S23), which decreased to 90 % upon re-emulsification and incubation between 3 – 6 h. We further observed significant cell death for long term incubation in W/O droplet with viability decreasing to ~30 % after 18 h, which can be attributed to the depletion of nutrients and accumulation of waste (Figure S23). We selected 6 h as the optimal incubation time to balance maximizing protein secretion while maintaining cell viability. It is noteworthy that dead cell stains, such as ethidium homodimer-1, which label available double stranded DNA, homogeneously labeled the BMPs and affected the measurement of the signal in the 561/590 nm channel. This homogeneous staining did not significantly affect decoding of the BMPs, but led to an increase in %CV (data not shown). Hence, we did not stain for dead cells for further analysis and we focused solely on viable cells.

We then evaluated the cytokine secretion of single THP-1 Mφ cells following LPS stimulation known to stimulate cytokine secretion by activating Toll-like receptor 4 (TLR4) signaling.[44] Firstly, THP-1 Mφ cells were co-encapsulated with cAb-BMPs in PiPs, washed and resuspended in medium supplemented with 10% FBS, 1% Pen/Strep, 25 mM HEPES and 2 mM $CaCl_2$, for both pH equilibration (pH 7.4) and nutrient supply. Next, we exposed PiPs to 100 ng mL^{-1} LPS and re-encapsulated them into W/O droplet to stimulate protein secretion and enable cytokine capture by the cAb-BMPs. Following incubation, we assayed the captured cytokines by MSA and used CLSM for assay readout. Here, PiPs were loaded into an imaging well plate and localized by supplementing 2MDa FITC-dextran to the buffer, acting as a negative stain, while the cells were stained with calcein-AM (Figure 5A). Since both FITC and calcein are imaged using the same Ex/Em condition, we purposely oversaturated calcein signals generated inside the cells' cytosol and applied variable thresholding on *Z*-projected images to sequentially segment PiPs and cells, allowing identification of cell-loaded PiPs (Figure 5B). Concurrently, BMPs were segmented based on their scattering signals (561/590 nm) and decoded based on their intensity barcode in the AF647 channel, while secreted

proteins were measured via the signals generated by the BV421 labeled SA (Figure 5C-D). For PiPs containing replicate BMPs targeting the same antigen, we summed the BV421 signals to account for the partitioning of proteins across distinct beads during capture. The microfluidic traps designed to immobilize PiPs in a microchannel with a step height reduction used in permeability testing (see Supplementary Note 3, Figure S13) were not employed for cell assays. Instead, we opted for an open well strategy for imaging, which unlike our current traps, allowed PIPs to arrange in a monolayer format without clogging. As such, spatial overlap of PiPs was minimized, allowing accurate co-localization of cells and BMPs in PiPs using the Z-projection of the FITC-dextran emission channel. In addition, the usage of commercial imaging well plate facilitated platform dissemination and simplified sample manipulations.

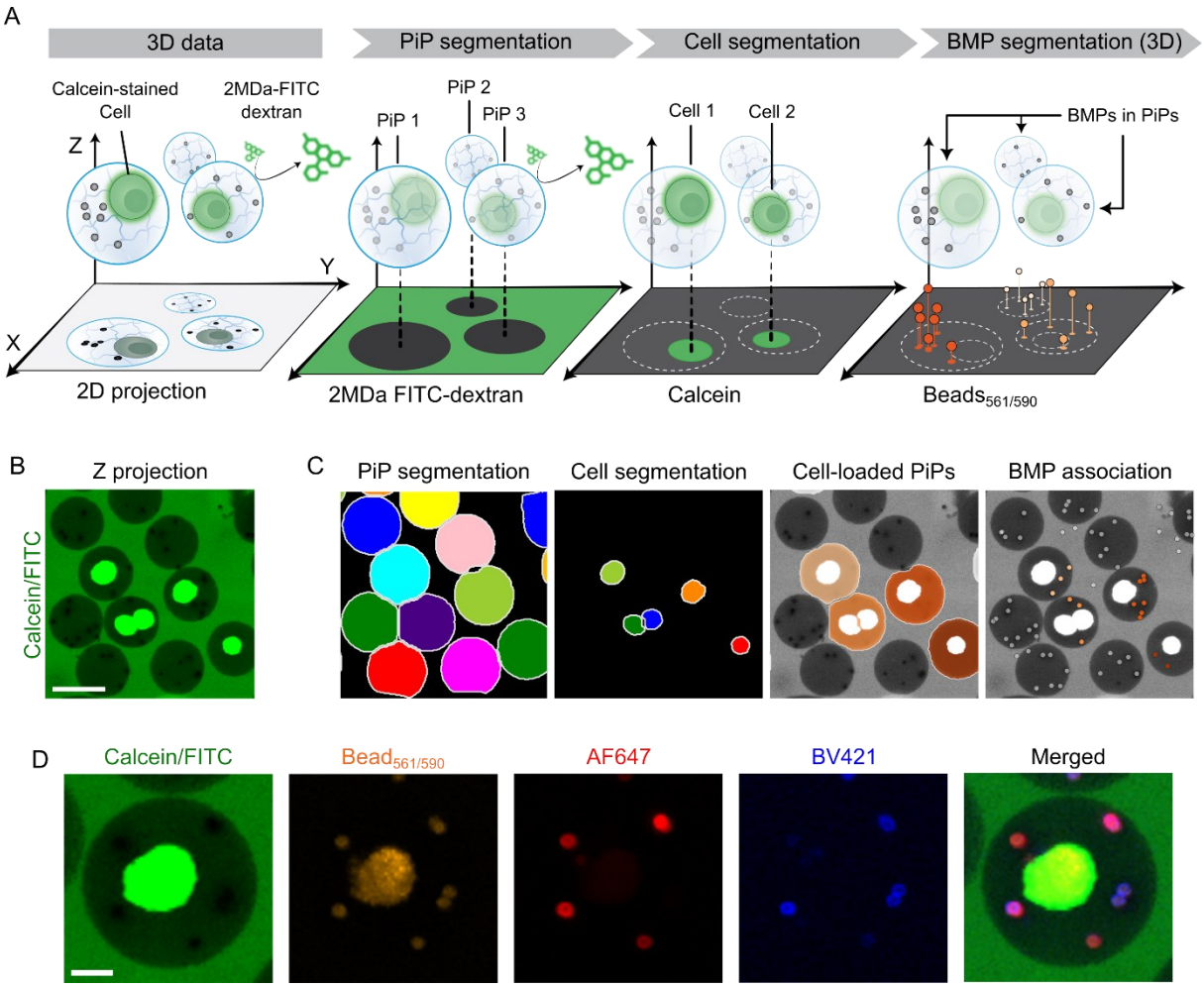

Figure 5: Segmentation of PiPs, viable cells and BMPs, followed by fluorescence quantification of barcodes and binding signals for PiP-plex assays. (**A**) Schematic overview of PiP segmentation and BMP association. PiPs immobilized on a poly-lysine coated coverslip and encapsulated cells are sequentially segmented from the Z-projection using a single fluorescence channel (FITC/Calcein). BMPs are segmented directly in 3D space based on their scattering signal at 590 nm, and associated with a specific PiP through their *XY*

coordinates and PiP contour. (**B**) Z-projection image used for segmentation. Viable THP-1 cells are labeled by calcein-AM, which diffuses through the PiPs and across the cell membrane, while a high molecular weight FITC-labeled dextran (2MDa) is excluded from the PiPs, enhancing the signal of the surrounding buffer. Scale bar: 50 µm. (**C**) Segmentation of image (B) with superposed masks. PiPs are initially segmented by applying a low pass threshold, followed by cell segmentation with a high pass threshold. Cell-loaded PiPs are identified by comparing the cell's coordinate to the PiPs' contour. BMPs are then associated with a specific PiP based on their coordinates. (**D**) CLSM images of a single PiP at different fluorescence channels. The Calcein/FITC channel was used to locate the cell and the PiP. The 561/590 channel was used for BMP segmentation. The AF647 fluorescence was used to assess intensity barcodes and associate them with specific proteins. Finally, BV421 fluorescence channel was used to record the binding signal. Scale bar: 10 µm.

Using PiP-plex, we measured an increased secretion of MIP-1α, TNF-α, IL-17A and IL-2 in THP-1 Mφ cells stimulated by LPS compared to non-stimulated controls (Figure 6A) which is in good agreement with secretion profile reported by Ma et al.[2] We validated our findings by bulk measurements of cytokines in the supernatant from LPS-stimulated and unstimulated control cells cultured in well plates in the absence of alginate. The measurements were performed using antibody microarrays with the same antibody pairs employed for PiP-plex analysis. While perfect consistency is not expected due differences in assay formats (i.e., single cells vs. bulk measurements, different LOD cut-offs, and potential statistical sampling biases), we anticipate replicating key findings. For both PiP-plex and antibody microarrays, only assay signals surpassing the LOD for each cytokine were considered in the assessment of statistical significance. Both platforms detected highly significant differences in secretion of MIP-1α and TNF-α following LPS stimulation (Figure S24-25 vs Figure 6A). IL-17A was also highly differentially secreted when assayed in PiP-plex, but since it did not reach the LOD on the microarray, the secretion differences could not be measured. Interestingly, IL-5 exhibited significant differential secretion in bulk, but not in the PiP-plex assay (Figure 6A, Figure S24), possibly because most single-cell measurements were below the LOD. For IFN-γ secretion, which was detectable in the PiP-plex assay but did not show significant differences, values above the LOD could not be measured in the bulk assays.

We assessed polyfunctionality of 527 single THP-1 cells by enumerating those that secreted more than one cytokine above the assay LOD (Figure 6B). Without stimulation, approximately 10 %, 6 %, 3 % and 2 % of 284 cells secreted 2, 3, 4 or more than 5 different cytokines, respectively. In contrast, after LPS stimulation approximately 23 %, 15 %, 6 % and 5 % of 243 secreted 2, 3, 4 or more than 5 different cytokines, respectively. In both cases, cytokines are part of various immunological programs, acting as effector, regulatory,

stimulatory or inflammatory molecules. Our results demonstrated that following LPS stimulation, a larger proportion of cells secreted cytokines above the assay LOD, as quantified by the polyfunctional strength index (PSI; Figure 6C). Alongside polyfunctionality, we evaluated the proportion of non-secreting cells and those secreting a single cytokine, based on whether the assay signal was below or above LOD, respectively. We noted an increase in the number of secreting cells upon stimulation (Figure 6D). Specifically, TNF-α and MIP-1α secretion increased 2 to 3- fold following LPS treatment, while the proportion of cells secreting other cytokines remained unchanged. For cells secreting at least 2 distinct cytokines, the cytokine contribution and individual profiles showed notable differences (Figure S26). Secretion profiles indicated both a greater number of polyfunctional cells and an increase in the amount of cytokines secreted by the LPS-treated cells, which is also reflected in the increase in the PSI. Overall, PiP-plex enabled the assessment of cellular polyfunctionality while retaining cellular viability.

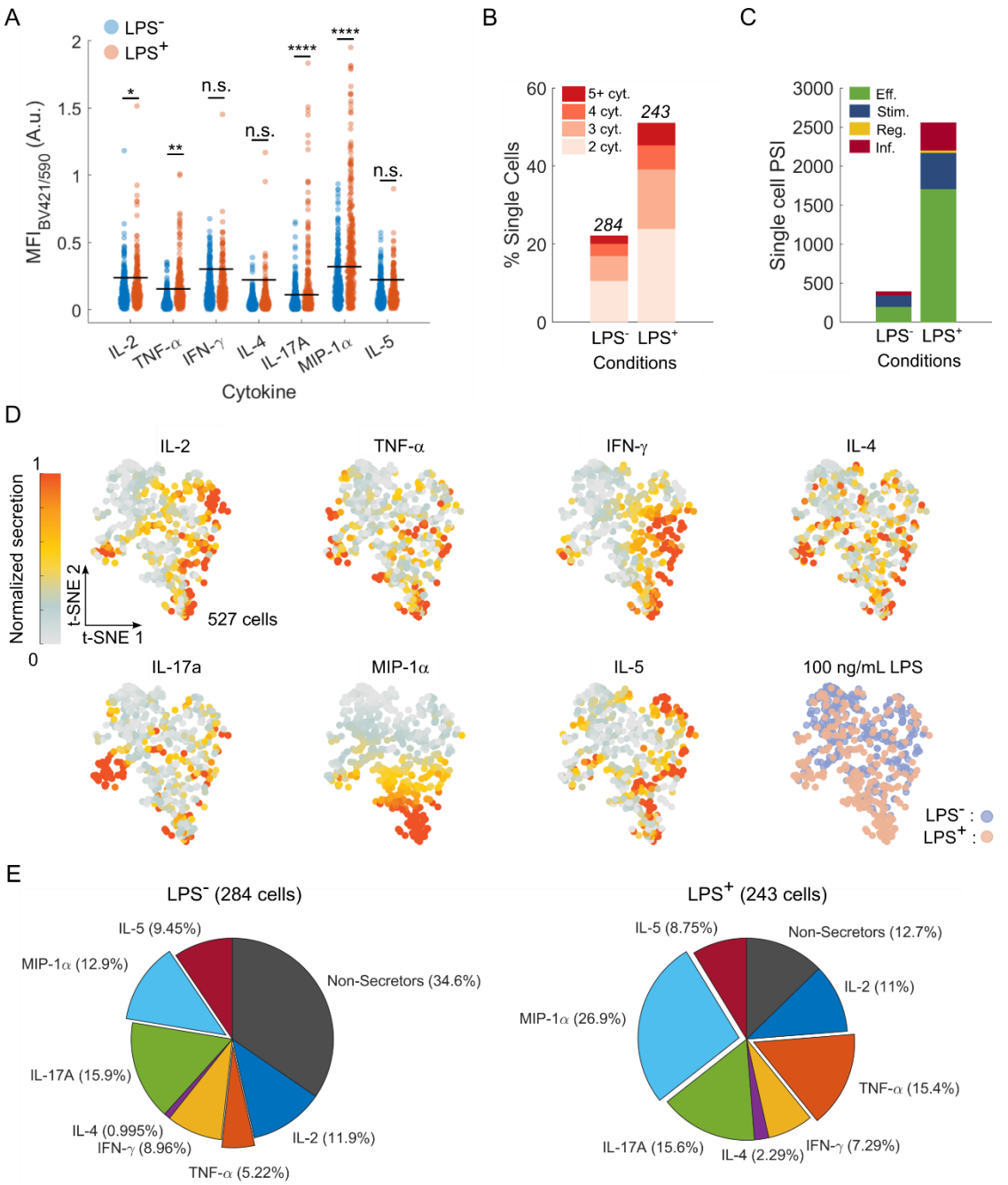

Figure 6: Single-cell quantification of secreted protein by THP-1 Mφ cells via PiP-plex. (**A**) Scatter plots showing BMP signal measurements from THP-1 Mφ cells in PiPs upon stimulation with 100 ng mL^{-1} LPS. ns: not significant; * $P < 0.05$, ** $P < 0.01$, **** $P < 0.0001$ by Mann-Whitney two-tailed test. Black lines represent the assay's LOD, calculated as three times the standard deviation above the background of PiPs containing no cells. Comparison of cytokine secretion of non-stimulated and stimulated THP-1 Mφ cells represented in the form of (**B**) single-cell polyfunctionality shown as a proportion (%) of cells that secreted 2, 3, 4 or more than 5 cytokines above the assay LOD for the cells entrapped in PiPs containing at least 5 different cAbs-BMPs. The values above the bar correspond to the total amount of cells analyzed per condition, including non-secretors and single-cytokine secreting cells. (**C**)

Polyfunctional strength index (PSI, with Eff: Effector; Stim: Stimulatory; Reg: Regulatory; Inf: Inflammatory) from cells described in (**B**). (**D**) T-distributed stochastic neighbor embedding (t-SNE) of polyfunctional cells (527 cells) according to their secretion of the seven cytokines and (**E**) the distribution of cytokine secretions with exploded views of TNF-α and MIP-1α to highlight the fold changes in secreting cell populations.

Discussion

We introduced a novel strategy to encode and anchor cAbs onto MPs using dsDNA. We generated up to seven distinct single-color BMPs with our novel construct (Figure 3) for subsequent single-cell MSA of secreted proteins. Our strategy supported the conception of various antibody panels for tailored single-cell immunoassays utilizing commercially available and validated antibody pairs for ELISA. It also supported the use of various fluorescent dyes, including small organic dyes and large polymeric dyes such as Brilliant Violet®, for assay signal generation (Figure S13). We developed an image processing pipeline enabling the segmentation of individual BMPs in 3D by CLSM which emulated single-particle signals acquired by FCM, for both immobilized BMPs onto coverslips and BMPs formulated into 50-µm-diameter PiPs. Our pipeline alleviates spatial restriction in *Z-axis* encountered in imaging FCM and supported MSA at the single-cell level. Our multiplexing capability surpasses other well established single cell secretomic platforms based on optofluidic technology[45, 46], and confined microenvironment such as droplets[7, 9] or nanovials[24] by 2- to 3-fold, all while maintaining cellular viability. Multiplexing could be further increased in PiP-plex by introducing additional fluorophores (i.e. $dsEO_i$) for barcoding, such as ATTO750, as previously developed.[27] However, the formulation of PiPs follows Poisson statistics, meaning that as multiplexing increases, the probability of generating PiPs with the full panel of cAb-BMPs decreases. Additionally, statistical factors impact the effective throughput of PiP-plex compared to other methods. Currently, we acquire 4-color *Z*-stack images (320 x 320 μm^2) composed of 35 slices in approximately 25 s. On average, each of these *Z*-stacks comprises 14 PiPs, with 6 containing exactly one cell. In addition, ~35 % of imaged PiPs contain the 7-plex panel. On average, 2 PiPs encapsulate both one cell and the full 7-plex panel per field of view. Thus, using our current setup, we could image and quantify the secretion of ~1000 cells per hour, while retaining >90 % cell viability. While this approach rivals other microfluidic chip-based methods[2], we envision that by integrating high-throughput microfluidic technologies, using inertial focusing for BMPs and/or single cells, will further enhance the platform's throughput by increasing the probability of simultaneous encapsulation of the full 7-plex panel with single cells.

Overall, the use of alginate as a hydrogel for our PiPs enhanced MSA performance (Figure 4) resulting in lower LODs and wider dynamic range compared to bulk assays. This improvement was attributed to the confinement effect of the hydrogel which increased both the apparent local protein concentrations and the collision frequency between molecules, as discussed by Moorthy *et al.*[47] Moreover, confinement favors protein association over dissociation due to favorable entropic contribution via molecular crownding.[48] We speculate that alginate, a natural polysaccharide, binds some cytokines, due in part, but not exclusively, to its intrinsic isoelectric point. Cytokine binding to alginate was more pronounced for IFN-γ, IL-4, MIP-1α and IL-5, which are known for binding to GAG in the extracellular matrix, consistent with the increased assay background and lower assay performance (Figure 4). Alternative hydrogels, such as agarose—widely used for single-cell assays[6, 49]—could be explored for generating PiPs due to its high mechanical stability and excellent diffusivity for antibody and proteins, potentially enhancing MSA performance. However, agarose was reported to affect cytokine secretion and may prevent retrieval of cells for downstream processing.[50] Therefore, the hydrogel composition should be tailored to the specific application, with its impact on cellular response fully evaluated. Additionally, careful validation of assay performance and antibody pairs is essential, particularly in the context of MSA of secreted proteins at the single-cell level, where protein concentrations are low and require antibodies with high affinity, specificity and minimal cross-reactivity.[35]

As a proof-of-concept, PiP-plex was used to quantify proteins secreted by differentiated THP-1 cells (Figure 6). We measured an increased secretion of TNF-α, IL-17A, IL-2 and MIP-1α upon LPS stimulation compared to the unstimulated control. We noted a good agreement between single cells (PiP-plex) vs bulk (antibody microarrays) measurements for the proteins that showed high differences in secretion and were well-above the LOD on both platforms, which included TNF-α and MIP-1α. IL-17A was highly secreted as measured by PiP-plex, but below the LOD on microarrays, while IL-5 was only differentially secreted as measured by microarrays. We believe that the confinement in a 65 pL volume W/O droplet helped increase the local concentration of IL-17A, exceeding the LOD in PiPs. Alginate saccharides were reported to suppress expression of IL-5 and IL-4 associated factor in T helper 1, and 2 cells,[51] which could account for the absence of significance in IL-5 signal in PiP-plex compared to the antibody microarray. Besides the non-specific binding of cytokines mentioned above, alginate is also known to induce immunological responses via TLR4[52] which is also activated by LPS. Furthermore, Ca^{2+}-crosslinked alginate gels leach Ca^{2+} ions, which may trigger an inflammatory response from immune cells, as reported by Chan *et al.* in dendritic cells.[53] These inherent aspects of alginate could be responsible for the activation of LPS^{-} cells and increased cytokine secretion in this cell population. Basal cell activation could be optimized in

the future by adjusting alginate composition, gelation conditions, and by chemical modification of the alginate, for example with an immunomodulatory peptide.[54]

We assessed the functional diversity of PMA-differentiated THP-1 cells using PiP-plex, all while preserving cell viability. We detected approximately 65 % of cells secreting at least one cytokine above the LOD in the LPS^- sample, and around 88 % in the LPS^+ sample (Figure 6E), proportions that are higher compared to those observed in other single-cell platforms.[24] This discrepancy may be due to an improved LOD of PiP-plex, heightened basal stimulation of cell secretion by alginate, or a combination of both. We detected the expected changes in secreted cytokines (Figure 6, and Figure S24) from THP-1 cells upon LPS treatment that vastly exceeded the threshold statistical significance, along with distinct t-SNE clustering of IL-17A and MIP-1α secreting cells. These findings both validate and illustrate the potential of PiP-plex. We also found that TNF-α was not secreted standalone, but rather co-secreted with other cytokines, concordant with the literature on LPS stimulated THP-1 cells.[2, 5] Further, these three cytokines overlap with the cluster associated to the LPS^+ condition. Likewise, cells secreting IL-2, IL-5, and IFN-γ were predominantly mapped to the right of the t-SNE graph, but failed to form well defined clusters, reflecting overall low secretion of these cytokines, and weak association with either LPS^- and LPS^+ conditions. Overall, we envision that PiP-plex could open multiple new investigative avenues, such as characterizing the secretome signature of various cells, studying the effect of extracellular ligand binding on the secretome, co-encapsulating multiple cell types in PiPs to investigate the effect of cell-cell contact and paracrine signaling effects on secretion;[34] and conducting all of these investigations while preserving cell viability, allowing retrieval of selected cells for further analysis and clonal expansion.

Materials and Methods:

Materials: A complete list of biological and chemical reagents is available in the supporting information (SI, Table S1, S2 and S3). All DNA sequences were acquired directly modified from Integrated DNA Technologies (IDT) with HPLC purification. THP-1 cells were a gift from Prof. Nicole Li-Jessen (McGill University).

Preparation of the precursor solutions: 1 M EDDA solution was prepared freshly by dissolving EDDA in 100 µL of 1 M NaOH with sonication, while 1 M $Zn(CH_3CO_2)_2$ solution was prepared freshly in 100 µL of MilliQ water. The resulting solutions were then mixed in a 1:1 ratio, thoroughly mixed by vertexing and incubated for 5 min to allow the generation of the ZnEDDA complex. Then, 42 µL of the ZnEDDA solution was mixed with 20 µL of 1 M MOPS pH 7.0, 167 µL of alginate 3 wt% in MilliQ, 5 µL of 1 vol% Tween-20 in MilliQ and 224 µL of either completed RPMI-1640 medium, or MilliQ water and vortexed, resulting in a final solution composed of 42 mM ZnEDDA, 40 mM MOPS pH 7.0, 1 wt% alginate, 0.01 vol% Tween-20 in RPMI-1640 of MilliQ water. A 200 mM stock solution of Ca-EDTA was prepared by dissolving both $CaCl_2$ and EDTA in MilliQ water, and the pH adjusted to 7.4 with concentrated NaOH.

DNA Antibody Conjugation, Purification and Quantification: To generate the DNA conjugated capture antibody (cAb-DNA), 200 µL (100 µg, 0.67 nmol) of 0.5 mg mL^{-1} antibody was buffer exchanged into pH 7.4 PBS and concentrated to a volume of ~20 µL (~5 mg mL^{-1}) using a 50k MWCO Amicon centrifugal filter (0.5 mL, Millipore Sigma). The antibody was diluted with 28 µL of PBS and mixed with 12 µL of a 1.67 mM Sulfo-SMCC (Thermo Fisher Scientific, USA) solution in 16.7% (v/v) DMSO in PBS, corresponding to a molar excess of 30:1 Sulfo-SMCC to antibody. Here, 10 mM stock solutions of Sulfo-SMCC were prepared in DMSO (aliquots stored at -20 °C) and diluted to 1.67 mM with PBS. The mixture was incubated for two hours at room temperature. Separately, 6 nmol of a 5' thiol modified DNA (Thiol Modifier C6 S-S; IDT) was incubated in 100 mM DTT solution in PBS and for 1 h 30 at room temperature to reduce the terminated thiol. The reduced DNA was then desalted twice by using two Zeba spin columns (7K MWCO, Thermos Fisher). The antibody-SMCC conjugate was desalted by using a single Zeba spin column. Then, the antibody-SMCC conjugate (75 µL) was mixed with the reduced thiol DNA (70 µL) and incubated for 1 h at room temperature followed by an overnight incubation at 4 °C. DNA antibody conjugated was purified using a 50k MWCO centrifugal filter to remove excess of unreacted DNA. The final antibody concentration was determined with a Pierce™ BCA protein assay (Thermo Fisher Scientific, USA) by adapting the *Micro-assay* from the manufacturer's instruction. Briefly, the volume of samples and reagents were reduced to 4 µL and mixed with 80 µL of assay reagent and incubated at 60 °C

for 5 min. Bovine gamma globulin standards (Thermo Fisher Scientific, USA) was employed as a standard for the assay. A typical protein recovery ~60-85 % was measured for the various antibody-DNA conjugate. Finally, the antibody-DNA conjugates were diluted to 1 mg/mL in pH 7.4 PBS without further purification and stored at 4 ^{o}C.

Generation of the intensity barcoded microparticles (BMPs): The generation of the barcoded microparticles (BMP) was based on the assembly of double stranded DNA on 2.7 µm diameter streptavidin-coated magnetic microparticles (DynaBeads M-270, Thermo Fisher Scientific, USA) as reported elsewhere.[27] First, fluorescently labeled double stranded encoder oligo (dsEO_i) were prepared by annealing 5' biotinylated oligos with 3' labeled oligos with dye *i* (EO_i). EO_0 was unlabeled, while EO_1 – EO_i was labeled with dye **1-*i***. To generate antibody anchored BMPs (cAb-BMPs), two different biotinylated oligos were used: a 21-nt space oligo (SO), and a 42-nt capture oligo (CO) which incorporate additional nts serving as an anchor for the oligo conjugated capture antibody (oligo-cAb). COs and SOs were separately annealed at 10 µM with individual EO_i at 80 ^{o}C for 5 minutes and cooled at 25 ^{o}C for 15 min in pH 7.4 PBS supplemented with 300 mM NaCl and 0.05% v/v Tween-20 (PBST0.05 + 300 NaCl), resulting in the generation of double stranded capture (dsCO_i) and double stranded space (dsSO_i) encoder oligos. Each dsCO_i were then mixed with their respective dsSO_i in a 2:7 ratio resulting in dsEO_i solutions for each *i* dye. The proportion of dsCO_i and dsSO_i allows fine tuning of the surface density of the cAb-DNA conjugate. A 25 µL volume of a given barcode was prepared by mixing the various dsEO_i at various proportions, such as dsEO_0 + dsEO_1 +…+ dsEO_i = 90 pmol, in PBST0.05 + 300 NaCl. Then, 25 µL containing 3.25 X 10^6 streptavidin coated microparticles in PBST0.05 + 300 NaCl was added and mixed rapidly by pipetting up-and-down to initiate the co-capture of the biotinylated dsEO_i onto the beads surface. Solutions were incubated for 90 minutes at room temperature on an orbital shaker at 950 rpm to prevent sedimentation of the microparticles (MPs). The resulting barcoded microparticles (BMPs) were washed three times with PBS supplemented with 0.1% v/v Tween-20 (PBST0.1) through cycles of magnetic aggregation and resuspension to remove uncaptured DNA. At this point, the BMPs may be kept, protected from light, at 4 ^{o}C until needed up to a period of one week.

Immobilization of the DNA-antibody conjugate on BMPs: BMPs were rinsed thrice with PBST0.05 + 450 NaCl and resuspend in a final volume of 50 µL. Then, 12.4 pmol of cAb-DNA in PBS were added to the BMPs (2:1 molar excess cAb-DNA to anchors on BMPs) and incubated for 30 min at room temperature on an orbital shaker at 950 rpm. After the pull-down of the cAb-DNA, the fully assembled cAb-BMPs were washed thrice with PBST0.01 and stored at 4 ^{o}C until needed for up to a week. Prior to the assay, the BMPs were blocked with 1% w/v

bovine serum albumin (BSA) and 1 mM biotin in PBST0.05 for 1 hour (or overnight) on an orbital shaker at 950 rpm and rinsed three times with PBST0.1 prior the assay.

Flow Cytometry and analysis: BMPs were detected using a ZE5 cell analyzer (Bio-rad, Ontario) with 488, 561 and 640 nm lasers employing 509/24, 577/15 and 670/30 band passes, respectively. Five thousand beads were measured per condition. Data were analyzed in MATLAB (v2022b, Mathwork) using custom-written codes. Briefly, single beads were segregated from doublets and other particles via their forward and side-scatter signal (FSC/SSC) and gated automatically by fitting a gaussian mixture model.

Confocal imaging: Fluorescent images of the BMPs, immobilized on surfaces or inside hydrogels (PiPs), were acquired using a Nikon eclipse Ti2 confocal microscope (Nikon, Japan) with a 20X (NA = 0.75) Plan Apo λ air objective (Nikon, Japan). The pinhole aperture was set to one 1.2 Airy Unit, and unless stated otherwise, the experiments were performed at room temperature. Digital offset of 10 (12 Bits images) was added to each fluorescent channel. For assaying by CLSM, *Z*-stacks, composed of 512 x 512 px^2 images with a 2X digital zoom, were acquired with a *Z*-step of 0.42 µm. Imaging was performed using a resonant *(bidirectional)* scanning mode and averaged 8 times with an overall integration time of 517.2 ms per frame (dwell time: 1.97 µs/pixel). Lasers were warmed up for at least one hour prior to the experiment to insure minimal laser fluctuation throughout the measurements. Four lasers (405/488/561/640) were used, along with 450/50, 525/50, 595/50 and 700/75 band pass, respectively. Channels were imaged pairwise to accelerate imaging by pairing 488/640 and 405/561 channels. These combinations provided minimal bleed-through. Imaging was performed via NIS-element AR (v5.42.04; Nikon, Japan).

3D-based image analysis: All data analysis was performed in MATLAB (v2022b, MathWork) using custom-written code available elsewhere (https://github.com/orgs/junckerlab/repositories/DropletAssay). BMPs were segmented and analyzed directly on three-dimensional data acquired by CLSM by adapting a 3D Hough transform developed by Xie et al.[29] available elsewhere (https://www.mathworks.com/matlabcentral/fileexchange/48219-spherical-hough-transform-for-3d-images). Briefly, the algorithm employs the spatial gradient to detect BMPs edges and estimate the individual bead center. Then, spherical masks, centered on each individual BMPs with a diameter of 3 µm, were generated and further segmented by a 3D watershed segmentation algorithm. The segmented masks were applied to the 3D images to integrate fluorescence intensity for all monitored Ex/Em channels. BMPs exhibited a strong signal emission in the 595/50 channel upon excitation at 561 nm wavelength, herein referred as the

$Bead_{590}$ channel, acting as a proxy of the scattering of individual BMPs. By employing the pseudo-scattering signal at 590 nm, BMPs were intensity-gated by imposing both a minimal and maximal intensity threshold corresponding to 85 % and 115 % of the median intensity distribution measured at 590 nm. This gating strategy eliminated false BMPs (i.e., false positive corresponding to bright detected individual pixels) and clustered BMPs resulting in poorly positioned spherical masks. Following intensity gating, intensity barcode identity of individual BMPs was determined by normalizing the AF647 measured signal by the pseudo-scattering $Bead_{590}$. Assay signal measured in BV421 channel were also normalized by the pseudo-scattering. This normalization accounted for discrepancy in position of BMPs in space and the imaged *Z*-plan, inducing small variation of the overall volume image on each bead. Experimentally, smaller %CV were obtained upon normalization by the scattering signal.

In silico design of BMPs: Due to the capability to generate independent barcodes through the usage of biotinylated oligos, barcode position and its resulting spectral bandwidth may be predicted and hence guide the development of spectral barcode exhibiting minimal overlaps (see Supplementary Note 2). Further details can be found elsewhere.[27] Briefly, four single-color BMPs were generated per fluorescent dye, with an increase proportion of $dsEO_{Dye}$:$dsEO_{unlabeld}$, and measured by CLSM and FCM as described above. These standards enabled the extraction of the irradiance μ_i of each dye, corresponding to the slope of the calibration curve, and the average %CV across all standards of the same dye. Using these two metrics, intensity barcodes were modeled assuming a constant %CV value for a given dye and imposing a minimal distance in between intensity barcodes corresponding to 3.5 times the measured standard deviation (See Figure S8), hence expecting to include over 99 % of a given BMPs from a gaussian distribution. We limited the total amount of oligos to be 90 pmol for barcodes. A total of 7 non-overlapping barcodes were modeled and validated experimentally (Figure 2C, Figure S8).

Automatic decoding of BMPs: Mixture of BMPs were automatically decoded based on their 2D intensity ($Bead_{590}$, AF647/$Bead_{590}$) via 2D clustering, analogous to Dagher et al.[27] Briefly, intensity data sets ***I*** were model with a gaussian mixture model (GMM) using the EM algorithm[55] to the probability distribution function given as:

$$p(\boldsymbol{I}) = \sum_{k=1}^{K} \pi_k \mathcal{N}(\boldsymbol{I}|\boldsymbol{M}_k, \boldsymbol{\Sigma_k})$$

where $\mathbf{M}_k$ and $\boldsymbol{\Sigma}_k$ are means and covariances of the *k* Gaussian given by $\mathcal{N}(\boldsymbol{I}|\boldsymbol{M}_k, \boldsymbol{\Sigma_k})$, respectively, and π_k is the mixing coefficient, corresponding to a normalized metric denoting how well BMPs fit the kth gaussian. *K* corresponds to the maximum number of unique barcodes to be decoded. Modeled intensity of each barcode was used as the initial value of the mean in

the GMM, $\boldsymbol{M}_k^0 = \boldsymbol{I}^{\boldsymbol{Model}}$. The initial covariance matrix value was a diagonal matrix with 10% CV in each dimension $\boldsymbol{\Sigma}_k^0$= diag(0.1 x $\boldsymbol{M}_k^0$), in accordance with our measured CV values. Initial clusters probabilities were considered homogeneous ($\pi_k^0 = 1/K$). When experimental data sets $\boldsymbol{I}$ are introduced, $p(\boldsymbol{I})$ measured the likelihood of that current data set to be fitted by the GMM clusters. Then, the probability ϕ of a given BMP ψ belonging to the cluster *k*, also referred to as the posterior probability, is calculated during the expectation step of the EM search using:

$$\phi_{\psi k} = \frac{\pi_k \mathcal{N}\left(\boldsymbol{I}_{\boldsymbol{\psi}} \middle| \boldsymbol{M}_k, \boldsymbol{\Sigma}_{\boldsymbol{k}}\right)}{p\left(\boldsymbol{I}_{\boldsymbol{\psi}}\right)}$$

We then performed a maximization step, where values of the Gaussian components ($\boldsymbol{M}_k, \boldsymbol{\Sigma}_{\boldsymbol{k}}$ and $\boldsymbol{\pi}_{\boldsymbol{k}}$) are updated to maximize the log-likelihood ln($p(\boldsymbol{I})$). The process was repeated for u to 5,000 iterations or until condition for convergence, defined as ln($p(\boldsymbol{I}_{\boldsymbol{i}})$) – ln($p(\boldsymbol{I}_{\boldsymbol{i-1}})$) < $1e^{-7}$, was reached. Finally, a posterior probability threshold, ranging from 60 to 80%, was applied, thereby eliminating BMPs with low ϕ.

Assessment of antibodies cross-reactivity in bulk: DNA-antibody conjugates were anchored on their respective BMP as described above and combined at a concentration of 100 BMPs per barcode per microliter. Prior to the assay, cAb-BMPs were first blocked with 1 mM biotin in PBST0.05 + 1% w/v BSA for 1 h and rinsed thrice with PBST0.1 via cycle of magnetic aggregation and resuspension in 100 µL of PBST0.1 using a liquid dispenser (MultifloFX, BioTek). For all experiments, incubations were performed in V-bottom 96-well microplate (Greiner bio-one, Germany) at room temperature with horizontal shaking at 950 rpm. Incubations with cytokines were performed for 120 min at a specific concentration (1 ng mL^{-1} or 100 ng mL^{-1}), rinsed thrice and incubated with dAbs for 1 h at 5 µg mL^{-1} and 2 µg mL^{-1} in assay buffer (PBST0.05 + 1% w/v BSA) for individual and cocktail incubation, respectively. BMPs were rinsed thrice and immobilized onto poly-L-lysine coated imaging 96-well microplate (Greiner-Bio-one) by incubating the BMPs for 10 min. Wells were gently rinsed with assay buffer and incubated for 60 min with 2 µg mL^{-1} BV421-labeled SA and rinsed thrice with PBST0.1 prior to imaging. BMPs were imaged by CLSM while being submerged by assay buffer. SNR_{dAbs} were calculated by subtracting cAb-BMP specific mean background in the absence of cytokine (*n* = *3*) from the calculated $MFI_{BV421/590}$ signals and normalized by the global standard deviation across all BMPs (*n* = 1*8*) of the SA background. Similarly, SNR_{Ag} were calculated by subtracting cAb-BMP specific mean assay background in presence of dAbs cocktail (*n* = *5*) from the calculated $MFI_{BV421/590}$ signal, and normalized by the global standard deviation of the assay background across all BMPs (*n* = *35*).

Microfluidic Device Fabrication: Microfluidic designs were drawn using Fusion 360 (Autodesk, 2022) and printed on a high-definition transparency photomask (50,800 DPI,

Fineline Imaging, Colorado Springs, CO). Microfluidics devices were fabricated with polydimethylsiloxane (PDMS) by standard soft lithography procedures.[56] Briefly, 35 µm layer of SU-8 (GM 1060 negative resin, Gersteltec, Engineering Solution, Switzerland) was spin-coated onto a 6-inch silicon (Silicon Quest International, Santa Clara, CA) wafer. Following soft baking, the photomask was aligned onto the wafer and was exposed to UV light at 365 nm (Hg i-line). Subsequently, the SU-8 was post-baked and developed in propylene glycol monomethyl ether acetate (PGMEA; Sigma-Aldrich, Oakville, ON) for 5 min. Following hard baking, the silicon mold was ready for the subsequent steps. Note that all pre-bake, post-exposure bake, and hard bake steps were performed using the standard temperature and time ramps on a programmable hot plate (HS40A, Torrey Pines Scientific, CA). The resulting mold was used for downstream fabrication of PDMS replica without further functionalization. To generate devices, mold was inserted into a laser cut circular hollow plate made of PMMA and immobilized using extra tack Frisket film (Grafix, Amazon), similarly reported by Li et al. (Chips and Tips; A Simple and Economical Holder for Casting PDMS Chips). Then, a 10:1 ratio of PDMS and curing agent were vigorously mixed, degassed for one hour under vacuum, poured onto the mold and cured for at least three hours at 65 ºC. PDMS was then cut and peeled off from the mold. Inlets and outlets holes were punched using a 1.2 mm biopsy punch (Harris Uni-Core™, Ted-Pella, Inc). Glass slides (75 x 50 mm) were cleaned with isopropanol with sonication for 5 minutes and thoroughly dried using nitrogen gas. Both glass slides and PDMS devices were activated for 35 seconds with an air plasma (Plasma Etch, Inc., NV) with 300 mTorr pressure and 150 mW power and bonded together. Devices were incubated at 65 ºC overnight to strengthen the glass and PDMS bonding efficiency. Prior their use, devices were treated with a 0.22 µm filtered solution of 2% v/v trichloro(1H,1H,2H,2H-perfluorooctyl)silane (Sigma-Aldrich) in Novec 7500 (3M, Canada), rinsed with 0.22 filtered Novec 7500 and dried by pressured nitrogen blow.

Alginate microgel- and PiPs generation: Alginate microgels were generated by adapting the competitive ligand exchange crosslinking (CLEX) reported by Håti et al.[31] by droplet-based microfluidics. Briefly, two aqueous solutions were prepared: a zinc-rich solution composed of 42 mM ZnEDDA, 40 mM MOPS pH 7.0, 1% w/v alginate and 40 % v/v RPMI-1640 or MilliQ water, and a calcium-rich solution composed of 42 mM CaEDTA, 40 mM MOPS pH 7.0 and 1% w/v alginate and 40% v/v RPMI-1640 or MilliQ water (see *Preparation of the precursor solutions*). The continuous phase was composed of 2% w/w fluorosurfactant (Ran Biotechnologies, MA) in Novec 7500 fluorinated oil (3M, Canada). All solutions were 0.22 filtered and loaded in 1 mL luer-lock plastic syringe (BD) equipped with a ½ 23G blunt needle (McMaster Carr) with FEP tubing (1/16 OD, 1/32 ID; Cole Palmer) and introduced into the microfluidic device via neMESYS syringe pumps (Cetoni GmbH, Germany). Flow rates the two

aqueous solutions were set to 100 µl hr^{-1} and the continuous phase was set to 450 µl hr^{-1}. The produced W/O droplets were collected into a 1.5 mL Eppendorf on ice. To release the alginate microgels from the emulsion, the excess oil was removed, and 200 µL of releasing buffer (25 mM MOPS pH 7.4, 130 mM NaCl, 2 mM $CaCl_2$, 2% w/v BSA) was added on top of the emulsion. Then, the droplets were coalesced by introducing 150 µL of 20% v/v of 1H,1H,2H,2H-Perfluoro-octanol (PFO; Sigma-Aldrich) in Novec 7500 and vigorously mixed by pipetting to fully saturate the droplet surface, while minimizing perturbation of the top medium layer. Droplets were incubated for 10 min for complete release of the gels, which relocated to the top aqueous phase. Released gels were carefully resuspended by pipetting, collected and transferred into a new Eppendorf tube. Care was taken to prevent collection of oil. For the experiments with cells encapsulated inside the alginate microgels, the releasing buffer was substituted by 400 µL of completed RPMI-1640 medium supplemented with 2 mM $CaCl_2$. During droplet coalescence, droplets were incubated at 37 °C for 30 min. To generate PiPs, cells and/or BMPs were supplemented to one of the soluble alginate phases (e.g., BMPs in Zn-EDDA and Cells in Ca-EDTA). Cells and BMPs were not supplemented to the same alginate phase. When PiPs were formulated without cells, RPMI medium was substituted by MilliQ water.

Multiplex assays of cytokine in bulk and PiPs: DNA-antibody conjugates were anchored on their respective BMP at a concentration of 100 BMPs per barcode per microliter and blocked with 1 mM biotin and 1% w/v BSA in PBST0.05. For assay in PiPs, cAb-BMPs were rinsed thrice with 25 mM HEPES pH 7.4, 0.1% v/v Tween-20, 135 mM NaCl to remove phosphate buffer and formulated into PiPs as described earlier in MilliQ at a final concentration of 100 BMPs per barcode per µL. Following PiPs generation, PiPs were isolated in 600 µL tube and rinsed thrice with assay buffer containing 25 mM MOPS pH 7.4, 130 mM NaCl, 2 mM $CaCl_2$, 2% w/v BSA, through cycles of centrifugation at 400 G for 2 minutes, resuspension in 200 µL of assay buffer and incubated for 10 min on a rotary shaker at 350 rpm to enable diffusion. All rinsing steps for PiPs involved the same procedure, while incubations were performed in 600 µL tubes. For incubations in bulk (without partition) PiPs were pipetted into V-shaped 96 well plates and rinsed thrice by magnetic aggregation. Wells were sealed with adhesive PCR plate seals to minimize solvent evaporation (Thermo Fisher). To establish binding curves and LODs, cytokine mixtures were incubated for 120 min at the specified concentrations and rinsed. BMPs were incubated for 120 min with dAb cocktails at a concentration of 2 µg mL^{-1} per dAb and rinsed. In the case of cAb-BMPs in bulk, BMPs were immobilized on poly-L-lysine coated 96-well imaging microplate as described above while PiPs remained in their corresponding test tube. BMPs were incubated for 60 min to 2 µg mL^{-1} BV421-labeled SA and rinsed. PiPs were transferred into the same imaging well plates and both bulk BMPs and PiP were imaged by

CLSM as described above. SNRs were calculated by subtracting the specific cAb-BMP assay background $MFI_{BV421/590}$ ($n = 5$) and normalizing by the global standard deviation across all barcodes ($n = 35$) of the assay background.

Cell culture: Monocytes (THP-1, ATCC TIB-202™) were cultured in T75 flask RPMI-1640 medium (Gibco) supplemented with 2 mM glutamine, 10% heat inactivated fetal bovine serum (HI-FBS, Gibco) and 1% penicillin/streptomycin. Cells were cultured in suspension following manufacturer's recommended protocol at 37 °C and 5% CO_2 at 100% humidity. When needed, THP-1 cells at 1 x 10^6 cells mL^{-1} were differentiated by supplementing 25 nM (15 µg mL^{-1}) of phorbol-12-myristate-13-acetate (PMA; Sigma Aldrich) in completed RPMI-1640 and incubated for a period of 48 h to allow differentiations. Medium was then exchanged for completed RPMI and cells were allowed to rest for 24 h. Differentiation of cells was confirmed by light microscopy (Axiovert 40 CFL, Zeiss), where differentiated cells became adherent and exhibited important morphological changes. Cells were cultured up to passage 10 for the current study.

Cell viability assessment: In a 6 wells plate, cells (1 x 10^6 cells mL^{-1}) were differentiated with 25 nM PMA as described above. Following differentiation, cells were rinsed with PBS pH 7.4 and stained with Calcein-AM/Ethidium homodimer-1 (LIVE/DEAD Cell viability assay, ThermoFisher) based on manufacturer's procedure. When cells were entrapped in gels, 0.5 µL calcein-AM and 2 µL ethidium homodimer-1 stock solution (stock from manufacturers) were diluted into 1 mL of buffer composed of 25 mM MOPS, 130 mM NaCl, 2 mM $CaCl_2$. The gels were washed with 25 mM MOPS pH 7.4, 130 mM NaCl and 2 mM $CaCl_2$, centrifuged at 200 G for 1 min and resuspend in 100 µL of the daughter solution of LIVE/DEAD stain in MOPS buffer. Cells were incubated at room temperature for 30 min, protected from light, prior to confocal imaging. It is noteworthy that DEAD stains, which typically stain duplexed DNA, will stain the BMPs in a homogeneous way, leading to a strong fluorescence background in the bead (561 nm excitation) channel. Fluorescence images were analyzed with Fiji.[57] Each fluorescence channel was pseudo flat-field corrected employing BioVoxxel toolbox (https://doi.org/10.5281/zenodo.10050002), contrast enhanced (0.35), Otsu's thresholded, features were then dilated, watershed segmented and analyzed via the Particle Analyzer function (Fiji) by adjusting the minimal- and maximal area value to the targeted feature size (cells, gels, or satellite droplets). A circularity of 0.3 and 0.6 were fixed for cells and gels/droplets respectively.

Cell encapsulation in PiPs and sandwich immunoassay: Prior to performing single-cell immunoassays on THP-1 cells, Fc receptors on THP-1 cells were blocked for 10 min with 5 µL

of Human TruStain FcX (Biolegend) based on manufacturer's recommendation to reduce nonspecific adsorption of dAbs prior to their encapsulation in PiPs. Following blocking, adherent macrophage-like THP-1 cells were rinsed once with PBS and detached from the culture flask with TrypLE™ (Gibco) for 10 min at 37 °C. The suspended cells were diluted with completed RPMI-1640 and centrifuged at 300 G for 5 min. Cells were concentrated into 5 mL completed medium and counted. The desired number of cells were then centrifuged at 300 G for 5 min and resuspended 0.22 filtered Ca-EDTA rich alginate phase (42 mM Ca-EDTA, 40 mM MOPS pH 7.0, 1% w/v alginate, 40% v/v completed RPMI-1640) at a final concentration of 18 x 10^6 cells mL^{-1}. Independently, blocked cAb-BMPs were combined to a final concentration of 30 000 BMPs μL^{-1} per barcode and resuspended in Zn-EDDA rich phase (42 mM Zn-EDDA, 40 mM MOPS pH 7.0, 1% w/v alginate, 40% v/v RPMI-1640 and 0.01% v/v Tween-20. Each dispersed phase was loaded into 200 µL sterile pipette tip pre-loaded with Novec 7500 as described elsewhere (Figure S27).[58] Water-in-oil (W/O) droplets were generated with a flow focusing junction as described above. Droplets were collected on ice, excess of oil removed and coalesced with 20% v/v PFO in Novec 7500, and 400 µL of RPMI-1640 supplemented with 25 mM HEPES pH 7.4 and 2 mM $CaCl_2$ layered on top of the emulsion. Droplets were incubated at 37 °C during the droplet releasing process for a period of 30 min.

PiPs were centrifuged at 200 G for 1 min, resuspended in 400 µL of completed media RPMI-1640, 25 mM HEPES pH 7.4, 2 mM $CaCl_2$, and incubated for 5 min to enable diffusion in/out the gels. These steps were repeated 3 times to ensure adequate washing. To stimulate cytokine secretion by differentiated THP-1 cells, the 2 last washing steps were performed with a 2X LPS (200 ng mL^{-1}; Invitrogen) solution in completed RPMI-1640, 25 mM HEPES pH 7.4, 2 mM $CaCL_2$ and incubated for 2 min each round. Then, the gels were centrifuged at 200 G for 1 min and the supernatant removed. PiPs were re-emulsified by adding 150 µL of 2% w/w fluorosurfactant, and vigorously mixed by pipetting up and down, leading to the confinement of individual PiP. De novo droplets, now entrapping cells and BMPs inside PiPs, were incubated for 6 h at 37 °C in a closed Eppendorf tube. Following incubation, PiPs were released by droplet coalescence with 20% v/v PFO and placed on ice. Cell laden PiPs were diluted with assay buffer (25 mM MOPS pH 7.4, 130 mM NaCl, 2 mM $CaCl_2$ and 2 % w/v BSA), centrifuged at 4°C at 200 G for 1 minute, washed with 200 µL of ice-cold assay buffer and incubated 5 min on ice. These washing steps were repeated thrice.

Isolated PiPs were centrifuged at 200 G for 1 min, rinsed with 200 µL of ice-cold assay buffer and incubated for 5 min on ice trice. PiPs were diluted 1:1 on ice with dAbs cocktail for 120 min at a concentration of 4 µg mL^{-1} per dAb in assay buffer, rinsed trice (10 min incubation per wash) with ice-cold assay buffer, diluted 1:1 with 4 µg mL^{-1} BV421-labeled SA for 60 min on ice, and finally rinsed thrice (10 min incubation per wash) with ice-cold assay buffer. PiPs

were resuspended in assay buffer and loaded into an imaging 96-well plate and imaged by CLSM as described next.

Fluorescence confocal imaging of cell-loaded PiPs: To image cells, BMPs, and PiPs by CLSM, PiPs suspension was diluted 1:5 in assay buffer supplemented with 1 nM FITC-dextran (2MDa; Sigma-Aldrich) and 4 μM calcein-AM). The solution was then transferred into a 96 imaging well plate (Greiner-Bio-one) which has been coated with 0.1% w/v poly-L-lysine for 30 min, rinsed with MilliQ water and dried prior to the addition of the PiPs. PiPs were incubated 5 min to allow sedimentation and immobilization, while enabling the increase of calcein signal inside viable cell's cytosol. PiPs were imaged as described above at room temperature.

Fabrication of microfluidic traps by 3D printing-based replica molding: Microfluidic traps were used for permeability testing, but not for the assays. Microfluidic molds were designed in Fusion 360 (Autodesk, v2022), exported as .STL file for slicing in the third-party software CHITUBOX (CBD technology Ltd., v1.9.5) at a layer thickness of 20 μm. Slices were then uploaded to an Elegoo Mars 3 Pro masked stereolithography LCD 3D printer (ELEGOO, Shenzhen, China) equipped with a 405 nm light source. The molds were printed in Miicraft BV-002A resin (Creative CADworks, Canada, ON) with the following settings: *Bottom Layer Count: 5, Anti-Aliasing: On, Grey-Level: 2, Base Exposure Time (BET): 25, Layer Height: 20 μm, Layer Exposure Time (LET): 2.3 seconds.* Following 3D printing, molds were washed on the build plate with isopropanol to remove excess of uncured resin and dried with nitrogen. Molds were then submerged in an isopropanol bath for 30 min with gentle agitation on a rotary shaker, dried with nitrogen followed by 4 min of exposure in a UV chamber (CureZone MKII, Creative CADworks), baked at 65 ºC overnight and exposed to a second 4 min UV exposure. Degassed PDMS (10:1 ratio) was poured into the 3D-printed molds and cured overnight at 65 ºC. PDMS was then cut and peeled off from the mold. Inlets and outlets holes were punched using a 1.2 mm biopsy punch. Glass slides (25 x 60 mm) were cleaned with isopropanol with sonication for 5 min and thoroughly dried using nitrogen gas. Both glass slides and PDMS devices were activated for 35 s with an air plasma with 300 mTorr pressure and 150 mW power and bonded together. Devices were incubated at 65 ºC overnight to strengthen the glass and PDMS bonding efficiency. Prior to their usage, devices were plasma activated for 2 min and functionalized 0.1% w/v poly-L-lysine solution for 30 min. Devices were then rinsed with MilliQ water and dried by pressured nitrogen blow.

Permeability assessment of PiPs: PiPs encapsulating BMPs (~20 000 BMPs per microliter per barcode) were formulated by droplet-based microfluidic as described above in the absence of medium. PiPs were isolated from the oil phase and washed thrice with buffer (25 mM MOPS

pH 7.4, 130 mM NaCl, 2 mM $CaCl_2$) by centrifugation. PiPs were then resuspended in buffer supplemented with 1 nM 2MDa FITC-Dextran and perfused into the microfluidic trap at 10 µL min^{-1}. Once PiPs reached the trapping area (lower height of the microchannel), flow was stopped for 5 min. CLSM images were acquired to assess baseline fluorescence signal of the BMPs using the same optical configuration as described above. Then, buffer containing assay reagents (2 µg mL^{-1} BV421-labeled SA and 4 µg mL^{-1} AF488-labeled Goat anti-rabbit antibody (Invitrogen) in 25 mM MOPS pH 7.4, 130 mM NaCl, 2 mM $CaCl_2$ and 1 nM 2MDa FITC-Dextran was perfused at a rate of 10 µL min^{-1} while imagining PiPs at an interval of 5 min for a period of 1 h. BMPs signals were extracted for each time point and normalized by the maximum fluorescence value across all BMPs for each fluorescence channel. Data were then model with a 1D accumulation model, defined as $f(t) = A(1-exp(-(t_0-\lambda)/\tau)$ where A, λ and τ are fit parameters and t_0 is the time offset to account for the delayed perfusion of SA and Ab. The extracted value of τ corresponds to the characteristic diffusion constant.

Antibody microarray profiling of cytokines in cell supernatant: Antibody microarrays were employed to detect secreted cytokine by Mφ THP-1 cells in cell supernatants upon LPS post-differentiation stimulation. Briefly, antibody microarrays were patterned onto Aldehyde functionalized glass slides (PolyAn, Germany) using a sciFLEXARRAYER SX inkjet bioprinter (SCIENION GmbH, Germany) equipped with a single piezo dispense capillary nozzle with coating 1 (SCIENION). Prior to antibody immobilization, glass slides were inspected by fluorescence imaging with a InnoScan 1100 AL microarray scanner (Innopsys, France) at 532 Ex and 100% gain to assess the quality of the aldehyde functionalized glass slide. Pristine capture antibodies (Table S3) were diluted to 100 µg mL^{-1} in 15% v/v 2,3-butanediol (Sigma-Aldrich) and 1 M betaine (Sigma-Aldrich) in PBS pH 7.4. A Goat-anti rabbit (Thermo Fisher Scientific, USA) was diluted and added to the antibody panel to serve as negative control. Antibody solutions were spotted in 16 (2 x 8) subarrays of 100 (10 x 10) 100 µm spots size using 500 µm pitch value. Patterned glass slides were incubated overnight at room temperature and 70% humidity, washed thrice with PBST0.01 (while incubating 5 min in between washes on a rotary shaker). Then, the glass slides were blocked with 3% w/v BSA in PBST0.1 at room temperature, washed thrice with PBST0.1, dried and inserted within a 16-well ProPlate multi-well chambers (Grace Bio-Labs, OR) to enclose the fabricated antibody microarray. Cell supernatants (PMA^+/LPS^- and PMA^+/LPS^+) were sampled out after 3 h of LPS stimulation, 0.22 µm sterile filtered and incubated for 2 h on the antibody microarray at room temperature at 450 rpm on a rotary shaker. Blank and antigen standards (1pg mL^{-1} to 100 ng mL^{-1}) were prepared in completed medium (phenol-red free RPMI 1640, 10 % HI-FBS, 1% Pen/strep, 25 mM HEPES pH 7.4, 2 mM $CaCl_2$) to emulate cell conditions once entrapped in PiPs. Wells were washed thrice with PBST0.1, 3 % w/v BSA with 5 min incubations. A detection

antibody mixture (2 μg mL^{-1} per antibody; Table S3) in assay buffer (25 mM MOPS pH 7.4, 130 mM NaCl, 2 mM $CaCl_2$, and 2% w/v BSA) was incubated for 2 h onto the wells at room temperature at 450 rpm. Wells were rinsed thrice with assay buffer, labeled by incubating with 1 μg mL^{-1} AlexaFluor 647 labeled streptavidin in assay buffer for 1 h, protected from light at room temperature at 450 rpm. The wells were washed thrice, rinsed with MilliQ water, dried, and directly imaged on with an InnoScan 1100 AL microarray scanner. Images were exported as .TIFF files and quantified using ArrayPro software (Meyer Instruments, v4.5).

Assessment of polyfunctionality and multivariate analysis: Single cell data was extracted, analyzed, and visualized using custom written codes in MATLAB (v2022, MathWorks). Multicolor fluorescence z-stacks for the different cell samples were acquired as described above. From the Calcein/FITC channel, we localized both PiPs and cells. PiPs were located by calculating the minimal *Z* intensity projection. The projection was binarized via thresholding the image, segmented using a watershed algorithm leading to the localization of individual PiPs. Potential alginate aggregates or odd object were sorted out by eliminating detected object exhibiting a circularity value below 0.60. Conversely, cells were located by calculating the maximum *Z* intensity projection, followed by thresholding and watershed segmentation. Cell-containing PiPs were identified by comparing each cell's centroid to each detected PiP boundaries. PiPs containing more then two cells were excluded from further analysis. BMPs were segmented based on the 561/590 nm channel, and their fluorescence intensity in channel 561/590, AF647 and BV421 was integrated as described above, and associated to their PiPs of origin by comparing each BMPs *X* and *Y* positions to each PiPs boundary. Fluorescence intensities were corrected by subtracting the local background in each fluorescence channel. To prevent artefact due to bleed-through from the Calcein signal into the 561/590 nm fluorescence channel, BMPs located in *X, Y, Z* within area *X, Y* occupied by a cell (i.e. if a BMPs is located in 3D above or below a cell) were excluded from the analysis. Moreover, BMPs located outside of PiPs were further discarded.

Fluorescence intensity per BMPs were normalized by their respective 561/590 scattering signal. Then, normalized BMPs were gated by applying a lower and upper intensities thresholds based on the 561/590 signal corresponding, respectively, to 0.65 and 1.45 times the median value across all BMPs. Remining BMPs were decoded using a GMM as described above. Assay signal (BV421 channel), of BMPs encoding the same cytokine and co-entrapped within the same PiPs were summed to account for cytokine partitioning among BMPs. Data of BMPs signals entrapped in PiPs without cell were used to assess assay background level of each cytokine. These data were used to generate cytokine abundance histograms which were then fitted by a normal distribution. The mean and standard deviation of the distribution were used to calculate assay LOD for each cytokine, defined as 3 time the standard deviation above

the mean background. These LODs were used to segregate cytokine-secreting cells and non secretor cells. Further downstream analyses were restricted to PiPs entrapping, at least, 5 distinct cytokine-encoded BMPs for each condition. This insured that a minimum of 5 cytokines per cells would be measured in multiplexed per conditions. These data were then used for further multivariate analysis and assessment of the PSI of the cells.

The PSI is defined as the total functional intensity contributed by all polyfunctional cells, that are cells co-secreting at least 2 cytokines above their respective assay LOD. The PSI of each condition was computed as the percentage (%) of polyfunctional cells relative to all measured cells, multiplied by the sum of the mean fluorescence intensity of each assayed cytokines secreted by those cells[1]:

$$\mathrm{PSI}_{sample} = (\%\ \text{polyfunctional cells in sample}) \times \sum_{i=1}^{7} MFI_i$$

We presented PSI for each sample conditions as segmented bars highlighting contribution of each group of cytokines, namely effector, stimulatory, regulatory and inflammatory.

t-SNE analysis was conducted on 527 cells corresponding to PiPs encapsulating a single cell and at least 5 distinct cytokine-encoded BMPs. Due to the low number of variable (7 cytokines), dimension reduction by principal component analysis was not performed prior analysis. t-SNE was run using default parameter value using *tsne function* in MATLAB.

Statistical Analysis: For single cell assay using PiPs, statistical analysis was performed using Mann-Whitney two-tailed test while unpaired, two-tailed *t*-test was used for bulk assay by using MATLAB. Data were presented as mean ± S.D. The sample size of figures requiring statistical analysis is stated in the corresponding figure caption. For all statistical tests, confidence levels of $^{*}P < 0.05$, $^{**}P < 0.01$, and $^{****}P < 0.0001$ were used as the threshold values.

Acknowledgements: The funding was provided by the Cell and Gene Therapy Program, National Research Council Canada. We would like to thank Prof. Nicole Li-Jessen from McGill University for providing the THP-1 cells. We would also like to thank Hicham Saad and Michael Martin from Nikon (Ontario, Canada) for fruitful discussions and support for microscopy imaging. We thank Andreas Wallucks for help and discussion for the multivariate analysis.

Authors contribution: F.L., D.J., L.M., T.V., conceptualized the experiments. F.L. performed, acquired, and curated all data. F.L. Designed the microfluidic devices. B.M., and M.J.P. prepared the photomask. L.L. prepared the microfluidic master wafer. F.L. developed the image processing pipeline. F.L., Y.M., designed and 3D printed microfluidic traps. M.S., prepared the Antibody microarray. F.S., optimized the hydrogel purification., D.J. L.M, A.N and

T.V., acquired the fundings. D.J., L.M., and T.V. supervised the project. F.L. wrote the manuscript. All authors commented on the draft manuscript.

Conflict of interest: The authors declare no competing financial interests

Data Availability Statement: The data that support the findings of this study are available from the corresponding authors upon reasonable request.

Keywords: single-cell analysis, droplet-based microfluidics, hydrogel, alginate, fluorescence microscopy, sandwich immunoassay

References

1. Ma, C., Cheung, A. F., Chodon, T., Koya, R. C., Wu, Z., Ng, C., Avramis, E., Cochran, A. J., Witte, O. N., Baltimore, D., Chmielowski, B., Economou, J. S., Comin-Anduix, B., Ribas, A. and Heath, J. R. *Cancer Discovery* **2013**, *3*:418-29
2. Ma, C., Fan, R., Ahmad, H., Shi, Q., Comin-Anduix, B., Chodon, T., Koya, R. C., Liu, C.-C., Kwong, G. A., Radu, C. G., Ribas, A. and Heath, J. R. *Nat. Med.* **2011**, *17*:738-43
3. Lu, Y., Xue, Q., Eisele, M. R., Sulistijo, E. S., Brower, K., Han, L., Amir, E.-a. D., Pe'er, D., Miller-Jensen, K. and Fan, R. *Proceedings of the National Academy of Sciences* **2015**, *112*:E607-E15
4. Altschuler, S. J. and Wu, L. F. *Cell* **2010**, *141*:559-63
5. Rossi, J., Paczkowski, P., Shen, Y.-W., Morse, K., Flynn, B., Kaiser, A., Ng, C., Gallatin, K., Cain, T., Fan, R., Mackay, S., Heath, J. R., Rosenberg, S. A., Kochenderfer, J. N., Zhou, J. and Bot, A. *Blood* **2018**, *132*:804-14
6. Chokkalingam, V., Tel, J., Wimmers, F., Liu, X., Semenov, S., Thiele, J., Figdor, C. G. and Huck, W. T. S. *Lab on a Chip* **2013**, *13*:4740-4
7. Eyer, K., Doineau, R. C. L., Castrillon, C. E., Briseño-Roa, L., Menrath, V., Mottet, G., England, P., Godina, A., Brient-Litzler, E., Nizak, C., Jensen, A., Griffiths, A. D., Bibette, J., Bruhns, P. and Baudry, J. *Nature Biotechnology* **2017**, *35*:977-82
8. Gérard, A., Woolfe, A., Mottet, G., Reichen, M., Castrillon, C., Menrath, V., Ellouze, S., Poitou, A., Doineau, R., Briseno-Roa, L., Canales-Herrerias, P., Mary, P., Rose, G., Ortega, C., Delincé, M., Essono, S., Jia, B., Iannascoli, B., Richard-Le Goff, O., Kumar, R., Stewart, S. N., Pousse, Y., Shen, B., Grosselin, K., Saudemont, B., Sautel-Caillé, A., Godina, A., McNamara, S., Eyer, K., Millot, G. A., Baudry, J., England, P., Nizak,

C., Jensen, A., Griffiths, A. D., Bruhns, P. and Brenan, C. *Nature Biotechnology* **2020**, *38*:715-21

9. Portmann, K., Linder, A., Oelgarth, N. and Eyer, K. *Cell Reports Methods* **2023**, *3*:100502
10. Antona, S., Abele, T., Jahnke, K., Dreher, Y., Göpfrich, K., Platzman, I. and Spatz, J. P. *Advanced Functional Materials* **2020**, *30*:2003479
11. Wimmers, F., Subedi, N., van Buuringen, N., Heister, D., Vivié, J., Beeren-Reinieren, I., Woestenenk, R., Dolstra, H., Piruska, A., Jacobs, J. F. M., van Oudenaarden, A., Figdor, C. G., Huck, W. T. S., de Vries, I. J. M. and Tel, J. *Nature Communications* **2018**, *9*:3317
12. Dimatteo, R. and Di Carlo, D. *Lab on a Chip* **2022**, *22*:1576-83
13. Udani, S., Langerman, J., Koo, D., Baghdasarian, S., Cheng, B., Kang, S., Soemardy, C., de Rutte, J., Plath, K. and Di Carlo, D. *Nature Nanotechnology* **2023**, 10.1038/s41565-023-01560-7
14. Cheng, R. Y.-H., de Rutte, J., Ito, C. E. K., Ott, A. R., Bosler, L., Kuo, W.-Y., Liang, J., Hall, B. E., Rawlings, D. J., Di Carlo, D. and James, R. G. *Nature Communications* **2023**, *14*:3567
15. de Rutte, J., Dimatteo, R., Archang, M. M., van Zee, M., Koo, D., Lee, S., Sharrow, A. C., Krohl, P. J., Mellody, M., Zhu, S., Eichenbaum, J. V., Kizerwetter, M., Udani, S., Ha, K., Willson, R. C., Bertozzi, A. L., Spangler, J. B., Damoiseaux, R. and Di Carlo, D. *ACS Nano* **2022**, *16*:7242-57
16. Koo, D., Dimatteo, R., Lee, S., Rutte, J. d. and Carlo, D. D. *bioRxiv* **2022**, 10.1101/2022.04.28.489940:2022.04.28.489940
17. Bailey, R. C., Kwong, G. A., Radu, C. G., Witte, O. N. and Heath, J. R. *Journal of the American Chemical Society* **2007**, *129*:1959-67
18. Armbrecht, L., Müller, R. S., Nikoloff, J. and Dittrich, P. S. *Microsystems & Nanoengineering* **2019**, *5*:55
19. Dietsche, C. L., Hirth, E. and Dittrich, P. S. *Lab on a Chip* **2023**, *23*:362-71
20. Baret, J.-C., Miller, O. J., Taly, V., Ryckelynck, M., El-Harrak, A., Frenz, L., Rick, C., Samuels, M. L., Hutchison, J. B., Agresti, J. J., Link, D. R., Weitz, D. A. and Griffiths, A. D. *Lab on a Chip* **2009**, *9*:1850-8
21. Rutkauskaite, J., Berger, S., Stavrakis, S., Dressler, O., Heyman, J., Casadevall i Solvas, X., deMello, A. and Mazutis, L. *iScience* **2022**, *25*:104515
22. Nakagawa, Y., Ohnuki, S., Kondo, N., Itto-Nakama, K., Ghanegolmohammadi, F., Isozaki, A., Ohya, Y. and Goda, K. *Lab on a Chip* **2021**, *21*:3793-803
23. Fischer, K., Lulla, A., So, T. Y., Pereyra-Gerber, P., Raybould, M. I. J., Kohler, T. N., Yam-Puc, J. C., Kaminski, T. S., Hughes, R., Pyeatt, G. L., Leiss-Maier, F., Brear, P.,

Matheson, N. J., Deane, C. M., Hyvönen, M., Thaventhiran, J. E. D. and Hollfelder, F. *Nature Biotechnology* **2024**, 10.1038/s41587-024-02346-5

24. Koo, D., Mao, Z., Dimatteo, R., Noguchi, M., Tsubamoto, N., McLaughlin, J., Tran, W., Lee, S., Cheng, D., de Rutte, J., Burton Sojo, G., Witte, O. N. and Di Carlo, D. *Proceedings of the National Academy of Sciences* **2024**, *121*:e2320442121
25. Lee, S., de Rutte, J., Dimatteo, R., Koo, D. and Di Carlo, D. *ACS Nano* **2022**, *16*:38-49
26. Koo, D., Dimatteo, R., Lee, S., de Rutte, J. and Di Carlo, D. *bioRxiv* **2022**, 10.1101/2022.04.28.489940:2022.04.28.489940
27. Dagher, M., Kleinman, M., Ng, A. and Juncker, D. *Nat. Nanotechnol.* **2018**, *13*:925-32
28. Dagher, M., Ongo, G., Robichaud, N., Kong, J., Rho, W., Teahulos, I., Tavakoli, A., Bovaird, S., Merjaneh, S., Tan, A., Edwardson, K., Scheepers, C., Ng, A., Hajjar, A., Sow, B., Vrouvides, M., Lee, A., DeCorwin-Martin, P., Rasool, S., Huang, J., Erps, T., Coffin, S., Han, Y., Chandrasekaran, S. N., Miller, L., Kost-Alimova, M., Skepner, A., Singh, S., Carpenter, A. E., Munzar, J. and Juncker, D. *bioRxiv* **2023**, 10.1101/2023.04.17.535914:2023.04.17.535914
29. Xie, L., Cianciolo, R. E., Hulette, B., Lee, H. W., Qi, Y., Cofer, G. and Johnson, G. A. *Toxicologic Pathology* **2012**, *40*:764-78
30. Li, H., Leulmi, R. F. and Juncker, D. *Lab on a Chip* **2011**, *11*:528-34
31. Håti, A. G., Bassett, D. C., Ribe, J. M., Sikorski, P., Weitz, D. A. and Stokke, B. T. *Lab Chip* **2016**, *16*:3718-27
32. Bassett, D. C., Håti, A. G., Melø, T. B., Stokke, B. T. and Sikorski, P. *Journal of Materials Chemistry B* **2016**, *4*:6175-82
33. Clark, I. C., Fontanez, K. M., Meltzer, R. H., Xue, Y., Hayford, C., May-Zhang, A., D'Amato, C., Osman, A., Zhang, J. Q., Hettige, P., Ishibashi, J. S. A., Delley, C. L., Weisgerber, D. W., Replogle, J. M., Jost, M., Phong, K. T., Kennedy, V. E., Peretz, C. A. C., Kim, E. A., Song, S., Karlon, W., Weissman, J. S., Smith, C. C., Gartner, Z. J. and Abate, A. R. *Nature Biotechnology* **2023**, *41*:1557-66
34. Wheeler, M. A., Clark, I. C., Lee, H.-G., Li, Z., Linnerbauer, M., Rone, J. M., Blain, M., Akl, C. F., Piester, G., Giovannoni, F., Charabati, M., Lee, J.-H., Kye, Y.-C., Choi, J., Sanmarco, L. M., Srun, L., Chung, E. N., Flausino, L. E., Andersen, B. M., Rothhammer, V., Yano, H., Illouz, T., Zandee, S. E. J., Daniel, C., Artis, D., Prinz, M., Abate, A. R., Kuchroo, V. K., Antel, J. P., Prat, A. and Quintana, F. J. *Science* **2023**, *379*:1023-30
35. Juncker, D., Bergeron, S., Laforte, V. and Li, H. *Current Opinion in Chemical Biology* **2014**, *18*:29-37
36. Simon Davis, D. A. and Parish, C. R. *Frontiers in Immunology* **2013**, *4*

37. Kemna, J., Gout, E., Daniau, L., Lao, J., Weißert, K., Ammann, S., Kühn, R., Richter, M., Molenda, C., Sporbert, A., Zocholl, D., Klopfleisch, R., Schütz, A., Lortat-Jacob, H., Aichele, P., Kammertoens, T. and Blankenstein, T. *Nature Immunology* **2023**, *24*:414-22
38. Vallet, S. D., Clerc, O. and Ricard-Blum, S. *Journal of Histochemistry & Cytochemistry* **2021**, *69*:93-104
39. Lortat-Jacob, H., Kleinman, H. K. and Grimaud, J. A. *The Journal of Clinical Investigation* **1991**, *87*:878-83
40. Lortat-Jacob, H., Garrone, P., Banchereau, J. and Grimaud, J.-A. *Cytokine* **1997**, *9*:101-5
41. Lipscombe, R. J., Nakhoul, A. M., Sanderson, C. J. and Coombe, D. R. *J Leukoc Biol* **1998**, *63*:342-50
42. Ali, S., Palmer, A. C. V., Banerjee, B., Fritchley, S. J. and Kirby, J. A. *Journal of Biological Chemistry* **2000**, *275*:11721-7
43. Lund, M. E., To, J., O'Brien, B. A. and Donnelly, S. *Journal of Immunological Methods* **2016**, *430*:64-70
44. Fan, J. and Malik, A. B. *Nature Medicine* **2003**, *9*:315-21
45. Mocciaro, A., Roth, T. L., Bennett, H. M., Soumillon, M., Shah, A., Hiatt, J., Chapman, K., Marson, A. and Lavieu, G. *Communications Biology* **2018**, *1*:41
46. Bronevetsky, Y. *Cytotherapy* **2020**, *22*:S119
47. Moorthy, J., Burgess, R., Yethiraj, A. and Beebe, D. *Analytical Chemistry* **2007**, *79*:5322-7
48. Minton, A. P. *Biopolymers* **1981**, *20*:2093-120
49. Fischer, K., Lulla, A., So, T. Y., Pereyra-Gerber, P., Raybould, M. I. J., Kohler, T. N., Kaminski, T. S., Yam-Puc, J. C., Hughes, R., Leiß-Maier, F., Brear, P., Matheson, N. J., Deane, C. M., Hyvönen, M., Thaventhiran, J. E. D. and Hollfelder, F. *bioRxiv* **2023**, 10.1101/2023.01.10.523494:2023.01.10.523494
50. Regier, M. C., Montanez-Sauri, S. I., Schwartz, M. P., Murphy, W. L., Beebe, D. J. and Sung, K. E. *Biomacromolecules* **2017**, *18*:709-18
51. Bang, M.-A., Seo, J.-H., Seo, J.-W., Jo, G. H., Jung, S. K., Yu, R., Park, D.-H. and Park, S.-J. *PLOS ONE* **2015**, *10*:e0117524
52. Jackson Hoffman, B. A., Pumford, E. A., Enueme, A. I., Fetah, K. L., Friedl, O. M. and Kasko, A. M. *Trends in Biotechnology* **2023**, *41*:1139-54
53. Chan, G. and Mooney, D. J. *Acta Biomaterialia* **2013**, *9*:9281-91
54. Vegas, A. J., Veiseh, O., Doloff, J. C., Ma, M., Tam, H. H., Bratlie, K., Li, J., Bader, A. R., Langan, E., Olejnik, K., Fenton, P., Kang, J. W., Hollister-Locke, J., Bochenek, M. A., Chiu, A., Siebert, S., Tang, K., Jhunjhunwala, S., Aresta-Dasilva, S., Dholakia, N.,

Thakrar, R., Vietti, T., Chen, M., Cohen, J., Siniakowicz, K., Qi, M., McGarrigle, J., Graham, A. C., Lyle, S., Harlan, D. M., Greiner, D. L., Oberholzer, J., Weir, G. C., Langer, R. and Anderson, D. G. *Nature Biotechnology* **2016**, *34*:345-52

55. Dempster, A. P., Laird, N. M. and Rubin, D. B. *Journal of the Royal Statistical Society: Series B (Methodological)* **1977**, *39*:1-22

56. Duffy, D. C., McDonald, J. C., Schueller, O. J. A. and Whitesides, G. M. *Analytical Chemistry* **1998**, *70*:4974-84

57. Schindelin, J., Arganda-Carreras, I., Frise, E., Kaynig, V., Longair, M., Pietzsch, T., Preibisch, S., Rueden, C., Saalfeld, S., Schmid, B., Tinevez, J.-Y., White, D. J., Hartenstein, V., Eliceiri, K., Tomancak, P. and Cardona, A. *Nature Methods* **2012**, *9*:676-82

58. Bounab, Y., Eyer, K., Dixneuf, S., Rybczynska, M., Chauvel, C., Mistretta, M., Tran, T., Aymerich, N., Chenon, G., Llitjos, J.-F., Venet, F., Monneret, G., Gillespie, I. A., Cortez, P., Moucadel, V., Pachot, A., Troesch, A., Leissner, P., Textoris, J., Bibette, J., Guyard, C., Baudry, J., Griffiths, A. D. and Védrine, C. *Nature Protocols* **2020**, *15*:2920-55